Paleocene (ca. 62 Ma) leucogranites in southern Lhasa, Tibet: products of syn-collisional crustal anatexis during slab roll-back?

Lin Ma[1, 2*], Qiang Wang[1, 3, 4*], Andrew C. Kerr[2], Jin-Hui Yang[5], Xiao-Ping Xia[1], Quan Ou[1], Zong-Yong Yang[1, 4], Peng Sun[1, 4]

[1] State Key Laboratory of Isotope Geochemistry, Guangzhou Institute of Geochemistry, Chinese Academy of Sciences, Guangzhou 510640, China

[2] School of Earth and Ocean Sciences, Cardiff University, Cardiff, Wales CF10 3AT, United Kingdom

[3] CAS Center for Excellence in Tibetan Plateau Earth Sciences, Beijing 100101, China

[4] University of Chinese Academy of Sciences, Beijing 100049, China

[5] Institute of Geology and Geophysics, Chinese Academy of Science, Beijing 100029, China

***Corresponding authors**

Telephone: + 86 20 85292337 (L. Ma); +86 20 85290277 (Q. Wang). Fax: +86 20 85290277 (Q. Wang). E-mail: malin@gig.ac.cn (L. Ma); wqiang@gig.ac.cn (Q. Wang)

ABSTRACT

Voluminous peraluminous leucogranites are common in large-scale orogenic belts and are crucial in gaining a fuller understanding of the related geodynamic process. However, the origin of such syn-collisional leucogranites remains highly controversial. In this contribution, we report petrological and geochemical data for Paleocene (ca. 63 Ma) garnet-bearing, two-mica granites and associated biotite granites from the Gangdese batholith in southern Tibet. The Zhengga biotite granites have high SiO_2 (70–73 wt %) and low MgO (0.4–0.7 wt %) contents with initial $^{87}Sr/^{86}Sr$ ratios of 0.7049 to 0.7050, $\varepsilon_{Nd}(t)$ values of +0.5 to +1.2 and zircon $\delta^{18}O$ values of 5.6‰ to 6.9‰, similar to most early Paleocene granitoids in southern Lhasa. These geochemical characteristics suggest that the Zhengga biotite granites were derived from a crustal source that mixed with variable amounts of Gangdese juvenile lower crust and minor ancient crust-derived melts. The Zhengga peraluminous, garnet-bearing, two-mica granites have similar Sr–Nd–O isotope compositions to the biotite granites (0.7037 to 0.7050, +0.4 to +0.8, 5.5‰ to 7.3‰, respectively) as well as higher SiO_2 (73–76 wt %) and lower TiO_2 (< 0.06 wt %), MgO (< 0.3 wt %), $Fe_2O_3^T$ (< 2 wt %) and CaO (< 0.7 wt %) contents. These most likely represent highly evolved biotite granite magmas that differentiated in the mid-crust. The first contact of India with Asia appears to have occurred in central Lhasa during the early Paleocene (65–63 Ma) and led to crustal thickening and cessation of magmatism. Early Paleocene slab rollback would have significantly enhanced asthenospheric corner flow and supplied a long-lived heat source for coeval crustal anatexis and metamorphism in southern Lhasa during the early phase of continental collision. Similar interaction between continental collision and oceanic subduction may also occur in other large-scale convergence zones in which the lithosphere and crust are

anomalously hot.

Key words: Early Paleocene; leucogranite; crustal anatexis; Tibet; Indo-Asian collision

INTRODUCTION

Leucogranites are a class of granite, usually with low (<5 vol.%) mafic mineral contents, that have been conventionally interpreted as the products of crustal melting. These granites are well-developed in collisional orogens and are characterised by high-silica and aluminium contents, and consequently usually contain aluminium-bearing minerals, such as garnet, tourmaline, muscovite and cordierite (Le Fort *et al*., 1987; Inger & Harris, 1993; Harrison *et al*., 1999; Patiño Douce, 2005; Brown, 2007; Zeng *et al*., 2011). This magmatic activity has been linked to a variety of geodynamic processes (e.g., crustal thickening, lithospheric delamination, back-arc extension, channel flow and mantle plumes (Harrison *et al*., 1997; Sylvester, 1998; Xu *et al*., 2008; King *et al*., 2011; Zeng *et al*., 2011). The crustal granitic melts represented by leucogranites can be used to help unravel the physical and geochemical response of the mid to lower crust to the changing tectonic regime during the evolution of a large orogen (e.g., Patiño Douce & Johnston, 1991; Harrison *et al*., 1997; Ding *et al*., 2005; Lee & Whitehouse, 2007; Zeng *et al*., 2011; King *et al*., 2011).

The Tibetan Plateau formed in response to the continental collision of India with Asia and arguably represents one of the most important tectonic events during the Cenozoic. In the Tibetan Plateau leucogranites have been conventionally interpreted as the result of crustal anatexis and are considered as petrologic evidence for collisional crustal processes, such as crustal flow, extension and thickening (Inger & Harris, 1993; Harrison *et al*., 1997; Ding *et al*., 2005; Lee & Whitehouse, 2007; Zeng *et al*., 2011; King *et al*., 2011). Most research on leucogranites in the orogen has focused on the more southerly Himalaya Block (Fig 1a). In comparison, relatively little work has been completed on the detailed syn-collisional geology along the

southern Lhasa block, which represents the southernmost part of the Asian continent. This southern Lhasa block is separated from the Himalaya Block by the Indus–Yarlung Tsangpo suture (IYTS) (Fig. 1a). In this contribution we focus on Cenozoic garnet-bearing two-mica granites and associated biotite granites in southern Tibet that potentially provide important constraints on the tectono-magmatic history of the orogen (e.g., Harrison *et al*., 1999; King *et al*., 2011; Zeng *et al*., 2011; Zhang *et al*., 2013).

A wide range of studies (using different dating methods) have presented evidence that the initial collision between India and Asia occurred in the early–middle Paleocene (ca. 65–58 Ma) (e.g., Klootwijk *et al*., 1992; Beck *et al*., 1995; Yin & Harrison, 2000; Ding *et al*., 2005; Leech *et al*., 2005; Cai *et al*., 2011; Yi *et al*., 2011; DeCelles *et al*., 2014; Wu *et al*., 2014; Hu *et al*., 2015). However, existing work on Early Paleocene isobaric high temperature granulite facies metamorphism and significant arc magmatism in southern Lhasa often do not support an early–middle Paleocene collision event (e.g., Chung *et al*., 2005; Guo *et al*., 2012; Zhang *et al*., 2013; Zhu *et al*., 2015). Thus, the detailed crustal evolution and related dynamic processes in southern Tibet during the initial collision stage (possibly in the early–middle Paleocene) are highly controversial. A significant amount of Paleocene magmatism has been discovered in southern Lhasa over the last 10 years (e.g., Wen *et al*., 2008; Ji *et al*., 2009, 2014; Lee *et al*., 2009; Guo *et al*., 2012; Jiang *et al*., 2014; Zhang *et al*., 2013). Consequently, an improved knowledge of the relationship between this Paleocene magmatism and metamorphic events during the Indo-Asian collision process will help our understanding of the origin of the magmatism and the processes involved in continental collision.

The Paleocene leucogranites found in the eastern syntaxis show evidence of

regional crustal anatexis and associated coeval granulite-facies metamorphism (Fig. 1b) (Guo *et al.*, 2012; Zhang *et al.*, 2013). Here we present detailed petrography, geochronology, major and trace element, and Sr–Nd–Hf–O isotopic data for the Zhengga leucogranites (garnet-bearing, two-mica granites) and associated biotite granites from the eastern segment of the Gangdese batholith. These new data suggest that large-scale Paleocene crustal anatexis likely occurred throughout southern Lhasa. U–Pb zircon dating of these granites yield Paleocene (ca. 63 Ma) ages and isotopic data show slightly depleted Sr–Nd isotopic compositions. These granites provide us with an excellent opportunity to constrain the origin of leucogranites and the role of Neo-Tethyan slab subduction and detailed syn-collisional crustal evolution processes during the onset of the India–Asia collision. A similar interplay between subduction and collision may be a common feature in large-scale continental collisional orogenic belts worldwide.

GEOLOGICAL BACKGROUND AND ROCK CHARACTERISTICS

The Himalayan orogen of South Tibet formed in response to the Indo-Asian collision and is composed essentially of Himalayan sequences and the south Lhasa Block. These are separated by the Indus-Yarlung Tsangpo suture zone, which contains mafic rocks representing the remnants of the Neo-Tethyan Ocean (Fig. 1a) (Yin & Harrison, 2000 and references therein). South of the Indus-Yarlung Tsangpo suture (IYTS) zone, two sub-parallel belts of Cenozoic leucogranites have been recognised, referred to as the High Himalayan (HH) and Tethyan Himalayan (TH) leucogranites (Fig. 1a). The High Himalayan leucogranites in the south form sheets, dykes, sills and laccolithic bodies that were emplaced along the South Tibetan Detachment System (STDS) (Le Fort, 1975; Le Fort *et al.*, 1987; Harrison *et al.*, 1999; Guo & Wilson, 2012). The

Tethyan Himalayan leucogranites are typically exposed in the cores of North Himalayan domes within the central Tethyan Himalayan physiographic region (~80 km north of the High Himalayan leucogranite belt) (King *et al*., 2011; Zeng *et al*., 2011; Liu *et al*., 2014). Previous research has shown that the High Himalayan leucogranites were generally emplaced during the latest Eocene–Middle Miocene from 35 Ma to 12 Ma (e.g., Coleman, 1998; Harrison *et al*., 1999; Guo & Wilson, 2012; Liu *et al*., 2014) whereas the Tethyan Himalayan leucogranites were primarily intruded between 45 and 7 Ma (e.g., Zhang *et al*., 2004; Ding *et al*., 2005; King *et al*., 2011; Zeng *et al*., 2011; Liu *et al*., 2014; Liu *et al*., 2016a, b; Wu *et al*., 2017). The Eocene leucogranites were derived by melting of thickened crustal materials and are found predominantly in the Tethyan Himalayan belt (e.g., Zeng *et al*., 2011; Liu *et al*., 2014).

The Lhasa Block was the last of a series of continental fragments accreted onto southern Asia during the Phanerozoic, before the collision of India (Allégre *et al*., 1984; Dewey *et al*., 1988; Yin & Harrison, 2000). Along the southern margin of the Lhasa Block (representing the southernmost part of the Asian continent), Late Triassic–Paleocene subduction of the Neo–Tethyan oceanic slab formed the Late Triassic–Early Tertiary Gangdese magmatic arc, comprising the Gangdese batholith and the Paleocene–Eocene Linzizong volcanic succession (e.g., Chung *et al*., 2005; Chu *et al*., 2006; Wen *et al*., 2008; Ji *et al*., 2009; Lee *et al*., 2009). The southern Lhasa sub-block (i.e., the Gangdese area) also contains minor Triassic–Jurassic volcano-sedimentary rocks (Fig.1a). Additionally, Late Devonian–Early Carboniferous granites have been recently discovered in the area. These have been interpreted to be derived from partial melting of ancient continental crust, and are characterised by negative $\varepsilon_{Hf}(t)$ values of zircon with T_{DM2} ages ranging from 1.90 to

1.40 Ga (Ji *et al*., 2012; Dong *et al*., 2014).

Significant Paleocene to mid-Eocene (65–41 Ma) magmatic activity with a major age peak at ca. 53–46 Ma occurred in the Gangdese magmatic arc (e.g., Yin & Harrison, 2000; Chung *et al*., 2005; Mo *et al*., 2006; Wen *et al*., 2008; Ji *et al*., 2009; Lee *et al*., 2009). This Paleocene–Eocene magmatism resulted from the tectonic transition from oceanic subduction to continental collision and is proposed to have been the result of both asthenosphere melting and crustal reworking (e.g., Chung *et al*., 2005; Mo *et al*., 2007; Ji *et al*., 2009; Lee *et al*., 2012; Zhang *et al*., 2013; Zhu *et al*., 2015). Limited data indicate that Paleocene medium- to high-grade metamorphic rocks, with associated leucogranites, mainly occur in the southeastern part of the Lhasa Block, especially in the Eastern Himalayan syntaxis (Guo *et al*., 2012; Zhang *et al*., 2013, 2015).

The Zhengga area is located in the Sangri County of Tibet and is less than 10 km north of the Yarlung-Zangbo suture zone (Fig. 1c). Large-scale granitic intrusive bodies, that are constituent parts of the Gangdese batholith, are found in the area (Fig. 1c). These granites were intruded into both the Lower Jurassic Yeba Formation and the Devonian plutons (Fig. 1c). The Paleocene granites consist of undeformed biotite granites and minor garnet–bearing two-mica granites (Fig. 2a, b).

The garnet-bearing two-mica granites and biotite granites generally exhibit massive and medium- to fine-grained (0.2–5.0 mm) granular textures, respectively (Fig. 2a, b). All these garnet-bearing granites have similar mineral compositions, which comprise quartz (~40–45 vol.%), K-feldspar (~25–30 vol.%), plagioclase (~15–20 vol.%), and subordinate garnet (~5 vol.%), biotite (~3–5 vol.%) and muscovite (~2–3 vol.%), with minor zircon, magnetite and daphnite (Fig. 2c–e; Table 1). Garnet crystals in the Zhengga garnet-bearing granites are euhedral or subhedral (Fig. 2c–e and g) and are

associated with feldspar, biotite, muscovite and quartz (Fig. 2c–e), suggesting that the compositions of garnet should be in equilibrium with these coexisting minerals. The intergrowth of plagioclase, biotite and muscovite also further support this (Fig. 2f). The Zhengga biotite granite, like the coeval Gangdese biotite granite, consists of plagioclase (~25–30 vol.%), alkali feldspar (~20–25 vol.%), quartz (~35–40 vol.%) and biotite (~5–10 vol.%) with minor Fe-oxides and titanite (Fig. 2h, i; Table 1). Biotite crystals in the Zhengga biotite granite can be divided into two types: (1) chloritised biotite, which is dark green both in plain and cross polarised light and (2) biotite, which is light brown in plain polarised light and green and yellow when viewed under cross polarised light. Plagioclase crystals commonly exhibit typical regular concentric growth zoning (Fig. 2h), and some plagioclase crystals are embedded in larger quartz grains. Microcline and perthite can be observed in garnet-bearing two-mica granites.

RESULTS

The least altered samples were selected for geochemical and isotopic analysis. Whole-rock major and trace element and Sr–Nd isotope data are given in Tables 2 and 3, respectively. Analytical methods, mineral composition data, laser ablation inductively coupled plasma mass spectrometry (LA-ICP-MS) and secondary ion mass spectroscopy (SIMS) zircon U–Pb geochronology and zircon Hf-O isotopic data for the Zhengga garnet-bearing granite and biotite granite samples are given in Supplementary Data Files 2–5.

Mineral geochemistry

Representative electron microprobe analyses of plagioclase, alkali feldspar, muscovite,

biotite and garnet are given in Supplementary Data File 3. The Zhengga garnet-bearing two-mica granites and biotite granites are characterised by markedly different mineral compositions.

The Zhengga biotite granites show a wide compositional range of feldspars including andesine ($An_{30-48}Ab_{51-69}Or_{1-11}$), oligoclase ($An_{12-30}Ab_{79-87}Or_{1-13}$), albite ($An_{1-3}Ab_{97-98}Or_{1}$), K-Na-feldspar ($An_{0–4}Ab_{12-42}Or_{58-85}$) and K-feldspar ($An_{0}Ab_{5-7}Or_{94-95}$), whereas feldspars from the Zhengga garnet-bearing two-mica granites consist mainly of oligoclase ($An_{10-21}Ab_{78-89}Or_{1}$), albite ($An_{3-9}Ab_{89-97}Or_{1-2}$) and K-feldspar ($An_{0}Ab_{2-5}Or_{95-98}$) (Supplementary Data File 3). Some plagioclase grains in the Zhengga granites show oscillatory compositional zoning (Fig. 3). Feldspars in the biotite granites have a core of alkali feldspar ($An_{0-4}Ab_{12-42}Or_{58-85}$) or andesine ($An_{30-48}Ab_{51-69}Or_{0-2}$) with a mantle or rim of oligoclase ($An_{17-29}Ab_{70-82}Or_{0-1}$). In contrast, feldspars in the garnet-bearing granites consist of a core of oligoclase ($An_{13-21}Ab_{78-86}Or_{1}$) and a rim of albite ($An_{6-9}Ab_{90-93}Or_{1-2}$) (Figs 3 and 4). Alkali feldspar from the Zhengga biotite granites is K-feldspar with a composition of $An_{0-4}Ab_{3-42}Or_{58-96}$ (Supplementary Data File 3). All these features suggest a crystallisation sequence of: andesine + K-Na feldspar (early), oligoclase + K-feldspar (later) and albite + K-feldspar (latest). In addition, plagioclases from the Zhengga garnet-bearing granites have mostly lower abundances of modal An (anorthite) compared to the biotite granites, suggesting a more evolved magma.

Biotites in the garnet-bearing two-mica granites are classified as lepidomelane with low to moderate MgO (4.3–6.8 wt %) and TiO_2 (0.2–1.2 wt %) contents, whereas biotites from the biotite granites are magnesian biotites with high MgO (9.6–10.8 wt %) and TiO_2 (2.1–3.1 wt %) (Supplementary Data File 3). Most of the muscovites in the Zhengga garnet-bearing two-mica granites are primary and also have low TiO_2

contents (0–0.57 wt %, most < 0.14 wt %, Supplementary Data File 3). All garnets in the Zhengga garnet-bearing, two-mica granites are magmatic pyralspite that consist of almandine and spessartine with minor pyrope and andradite ($Alm_{23-59}Sps_{36-64}Pyr_{1-5}And_{0-8}$, Supplementary Data File 3). The magmatic garnets from the garnet-bearing, two-mica granites exhibit similar compositional zoning and are characterised by increasing Mn, decreasing Fe and oscillatory Ca from core to rim (Fig. 5). In addition, all garnet grains have a narrow rim that is richer in Mn (Fig. 5).

Zircon U–Pb geochronology

Three garnet-bearing granite samples and three biotite granites were selected for zircon dating. Zircons in these samples have crystal lengths of ~150–300 μm and length:width ratios from 2:1 to 3:1. Zircon U–Pb isotopic data are given in Supplementary Data File 4. Well-developed oscillatory zoning and high Th/U ratios of zircons from the Zhengga granites indicate a magmatic origin (Hoskin & Black, 2000). U–Pb spot analyses on samples 11SR03, 11SR04 and 11SR05-1, yielded $^{206}Pb/^{238}U$ ages of 61 to 66 Ma (SIMS), 61 to 64 Ma (LA-ICPMS) and 58 to 65 Ma (SIMS), with weighted-mean ages of 62.6± 0.5 Ma (MSWD = 1.4), 62.7 ± 0.7 Ma (MSWD = 0.24) and 62.7 ± 0.8 Ma (MSWD = 2.0), respectively for the three biotite granite samples (Fig. 6a–c; Supplementary Data File 4). LA-ICPMS U–Pb spot analyses on samples 09TB66, 11SR01-2 and 11SR05-2, yielded $^{206}Pb/^{238}U$ data of 61 to 64 Ma, 55 to 63 Ma and 61 to 63 Ma, with weighted-mean ages of 62.2 ± 0.6 Ma (MSWD = 0.18), 57.4 ± 1.6 Ma (MSWD = 2.1) and 61.5 ± 0.6 Ma (MSWD = 0.22), respectively for the three garnet-bearing two-mica granites samples (Fig. 6d–f; Supplementary Data File 4). With the exception of a younger age of 57.4 Ma for the garnet-bearing, two-mica granite sample 11SR01-2, the other garnet-bearing,

two-mica granite and biotite granite samples show consistent zircon U–Pb ages ranging from 62.7 to 61.5 Ma, indicating that the Zhengga leucogranites and biotite granites were likely emplaced in the early Paleocene (ca. 62 Ma). It should be noted that some of the data for sample 11SR01-2 were excluded from Supplementary Data File 4 owing to possible loss of radiogenic Pb.

Major and trace element geochemistry

The Zhengga granite samples all have high SiO_2 contents, with the garnet-bearing, two-mica granites having higher SiO_2 and lower TiO_2, $Fe_2O_3^T$, MgO and CaO contents than the biotite granites (Table 2). All the Zhengga garnet-bearing granites have high K_2O (4.0–4.9 wt %) contents with markedly peraluminous compositions (A/CNK = molecular $Al_2O_3/(CaO+Na_2O+K_2O)$ = 1.03–1.21) and have similar major element compositions to Miocene High Himalayan leucogranites (Fig. 7). In contrast, the biotite granites are metaluminous to slightly peraluminous (A/CNK = 0.98–1.08) with relatively low K_2O (3.1–4.8 wt %) and high CaO (1.6–2.8 wt %).

The Zhengga granite samples exhibit a range of total rare earth element (REE) contents and are characterised by slightly to moderately enriched light REE with flat chondrite-normalised heavy REE patterns and variable negative Eu anomalies ($Eu/Eu^* = Eu_{CN}/(Sm_{CN}+Gd_{CN})^{1/2}$) (Fig. 8a). In more detail, the Zhengga garnet-bearing, two-mica granites show slightly enriched LREE patterns ($[La/Sm]_{CN}$ = 1.9–2.5) with significant negative Eu anomalies (Eu/Eu* = 0.1–0.2). In contrast, the biotite granites have more enriched LREE patterns ($[La/Sm]_{CN}$ = 2.7–4.1) with moderate negative Eu anomalies (Eu/Eu* = 0.5–0.9) that are not as marked as the garnet-bearing granites (Fig. 8a, Table 2).

On primitive mantle-normalised plots (Fig. 8b), the Zhengga granites are enriched

in large ion lithophile elements (LILE), such as Rb, Th, U and have slightly depleted high field strength elements (HFSE), such as Nb, Zr and Ti. They have negative Ti anomalies ($Ti/Ti^* = Ti_{PM}\times2/(Sm_{PM}+Tb_{PM})$ = 0.02–0.22) and variable Sr anomalies ($Sr/Sr^* = Sr_{PM}\times2/(Ce_{PM}+Nd_{PM})$ = 0.17–1.42). It should also be noted that the Zhengga garnet-bearing, two-mica granites have moderately negative Nb anomalies ($Nb/Nb^* = Nb_{PM}\times2/(Th_{PM}+La_{PM})$ = 0.23–0.60) but with relatively high $[Nb/La]_{PM}$ (0.72–1.69, mean 1.13) ratios, which are different from arc magmatic rocks.

Sr–Nd isotope geochemistry

Overall, the Zhengga granites have very similar initial $^{87}Sr/^{86}Sr$ ratios (0.7037–0.7050) and $\varepsilon_{Nd}(t)$ values (+0.43 to +1.15) (Fig. 9a; Table 3). These isotopic signatures distinguish the Paleocene granites from the Devonian granites as the latter have more enriched Sr-Nd isotopic compositions ($[^{87}Sr/^{86}Sr]_i$ = 0.7238 to 0.7470 and $\varepsilon_{Nd}(t)$ = -11.1 to -10.0; Table 3). Because of the variable $^{147}Sm/^{144}Nd$ of the Zhengga granites, two-stage Nd model ages (T_{2DM}) are used in this study (Liew & Hofmann, 1988). The two-stage Nd model age is an age at which the isotopic composition of the sample was identical to that of a model reservoir (most often CHUR or depleted mantle) and compensates for the effects of possible secondary Sm/Nd fractionation as a result of intra-crustal partial melting (Liew & Hofmann, 1988). In terms of two-stage Nd model ages (T_{2DM}) (based on the depleted mantle), the garnet-bearing granites and biotite granites yield almost the same results (1.04–1.08 Ga and 0.99–1.07 Ga, respectively) (Table 3).

Zircon Hf–O isotopic geochemistry

In situ zircon Hf isotope data for sample 09TB66 and O isotope data for samples

09TB66, 11SR01-2, 11SR04 and 11SR05-1 are listed in Supplementary Data File 5. Zircons from sample 09TB66 (garnet–bearing, two-mica granite) have positive $\varepsilon_{Hf}(t)$ values (+5.5 to +11.7), which are markedly higher than those of zircons from coeval S-type granites located near the Eastern Himalayan Syntaxis (Fig. 9c). In addition, zircons from sample 09TB66 also have young Hf model ages (0.27–0.52 Ga). All the Zhengga garnet-bearing granites and biotite granites have similar zircon $\delta^{18}O$ values (5.5‰ to 7.3‰) (Fig. 9d), which are slightly higher than those (5.3 ± 0.3‰) of igneous zircons in equilibrium with mantle-derived magmas (Valley *et al.*, 1998; Valley, 2003) (Fig. 9b).

DISCUSSION

Petrogenesis of the Zhengga granites

Biotite granites

The Zhengga biotite granites are characterised by high silica, moderate amounts of K_2O and low MgO contents with slightly peraluminous compositions and thus are unlikely to be derived from mantle-derived magma by fractional crystallisation. Crust-derived granitic magmas are either supracrustal (formed from metasedimentary rocks) or infracrustal (formed from igneous rocks that solidified at depth) in character; this is reflected in the S- and I-type notation used to describe these granites (White & Chappell, 1977; Kemp *et al.*, 2007). P_2O_5 is particularly effective in distinguishing between I- and S-type granitoids, since it decreases with fractional crystallization in I-type granites and increases with fractionation in S-type granites (Chappell & White, 1992). Decreasing P_2O_5 with increasing SiO_2 (Fig. 10c) suggests that both Zhengga granite types are I-type and not S-type granites.

In addition, although isotopic compositions overlap with I-types (Chappell & White,

1992), S-type granites have generally higher $\delta^{18}O$ and $^{87}Sr/^{86}Sr$ values with lower $^{143}Nd/^{144}Nd$ isotopic compositions. Unlike whole-rock data, zircon is able to preserve the magmatic O isotope composition (Peck *et al*., 2003), and igneous zircons in equilibrium with mantle-derived magmas have an average $\delta^{18}O$ value of 5.3 ± 0.3‰ (1SD) (Valley, 2003). This range is insensitive to magmatic differentiation, because the attendant rise in bulk-rock $\delta^{18}O$ is compensated by an increase in zircon/liquid $\delta^{18}O$ fractionation from +0.5‰ for mafic melts to +1.5‰ for silicic derivatives (Valley *et al*., 2005). Values of $\delta^{18}O$ in zircon above 5.6‰ thus fingerprint an ^{18}O-enriched supracrustal component in the magma from which the zircon crystallised, this being either sedimentary rock (10‰ to 30‰) or altered volcanic rock (up to 20‰) (Eiler, 2001, 2007). Given that intragrain heterogeneity of $\delta^{18}O$ usually does not exceed 1‰ (Kemp *et al*., 2007), the relatively variable and low zircon $\delta^{18}O$ (5.6‰ to 6.9‰) values of the Zhengga biotite granites therefore track the progressive interaction between two end-member components during zircon crystallisation, these being parental low $\delta^{18}O$ magmas and metasedimentary-derived materials.

The Latest Triassic to Cretaceous Gangdese granitoids have high and positive $\varepsilon_{Nd}(t)$ (up to +5.5) and $\varepsilon_{Hf}(t)$ (up to +16.5) values (Chu *et al*., 2006; Wen *et al*., 2008; Ji *et al*., 2009; Zhu *et al*., 2011; Ma *et al*., 2013b and references therein), indicating a juvenile crust beneath the southern Lhasa terrane. Because Late Cretaceous Zhengga gabbros that were intruded into the lower crust are also exposed in the same region (Fig. 1c; Ma *et al*., 2013b), we propose that the Gangdese juvenile crust represented by the Zhengga gabbros is the most likely source of the low $\delta^{18}O$ end-member (Fig.9b). However, it is significant that many magmatic rocks with relatively low $\varepsilon_{Nd}(t)$ and $\varepsilon_{Hf}(t)$ values were emplaced in the southern Lhasa terrane during the Paleocene (Fig. 9a, c). As mentioned above, due to their relatively high and variable zircon O isotope

and low $\varepsilon_{Nd}(t)$ values, a contribution from more enriched components to the source of the Zhengga biotite granites also needs to be considered. Sr-Nd isotope modelling reveals that subducted pelagic sediments, Indian crust and ancient Lhasa basement all are likely potential enriched end-members (Fig. 9a).

The Zhengga granitic magmas are unlikely to have experienced significant crustal contamination for the following reasons: (1) homogeneous $\varepsilon_{Nd}(t)$ (+0.4 to +1.2) and $(^{86}Sr/^{87}Sr)_i$ (0.7037 to 0.7050) values (Table 3), and the lack of correlation between $^{147}Sm/^{144}Nd$ and initial $^{143}Nd/^{144}Nd$ ratios (Supplementary Data File 6) (Vervoort & Blichert-Toft, 1999); (2) given that crustal components generally exhibit distinctly low $\varepsilon_{Nd}(t)$, MgO, low Nb/La and Nb/Th values and high $^{87}Sr/^{86}Sr$ ratios (Rudnick & Fountain, 1995), any crustal assimilation that occurred during magma ascent would have caused an increase in $(^{87}Sr/^{86}Sr)_i$ and a decrease in $\varepsilon_{Nd}(t)$ in the magma suites (e.g., Rogers *et al.*, 2000). The $(^{87}Sr/^{86}Sr)_i$, $(^{143}Nd/^{144}Nd)_i$ and Nb/La values of the Zhengga biotite granites show no significant correlation with increasing SiO_2 contents (Fig. 10e and Supplementary Data File 6), which is also inconsistent with significant crustal assimilation.

Previous studies have shown that melts derived from subducted oceanic sediment contain high concentrations of both Th and LREE (e.g., Hawkesworth *et al.*, 1997). However, the lack of significantly higher Th and LREE contents and or elevated Th/U ratios suggests insignificant involvement of oceanic sediment in the generation of the Zhengga biotite granites (Fig. 8; Table 2). The associated Devonian granites, (Figure 1c), are likely substantially derived from ancient Lhasa basement (Dong *et al.*, 2014), and thus are characterised by similar Sr-Nd isotopic compositions ($\varepsilon_{Nd}(t)$ = -11.1 to -11.0; $(^{87}Sr/^{86}Sr)_i$ = 0.7236 to 0.7274) (Fig. 9a; Table 3) to the Paleocene S-type granites in the Eastern Himalayan Syntaxis (Zhang *et al.*, 2013). We therefore favour

the involvement of ancient Lhasa basement in the generation of the Zhengga biotite granites. Modelling of equilibrium (batch) melting also indicates that the high degree (approximately 10% to 50%) melting of 95% Zhengga gabbro (Ma *et al*., 2013b) plus 5% two-mica granite can produce melts compositionally similar to the Zhengga biotite granites (Fig. 11), further supporting this model. The details of partial melt modelling are listed in Supplementary Data File 7. Alternatively, it is also possible that another crustal component, such as Indian continental crust (Jiang *et al*., 2014), might have contributed to the source of these granites, although lack of other solid evidence to support direct contact of India with this region during the early Paleocene would seem to preclude this possibility.

The Zhengga biotite granites also have moderately negative Eu anomalies (Eu/Eu* down to 0.5) indicating plagioclase and, or, K-feldspar fractionation. Fractionation of plagioclase would result in negative Sr–Eu anomalies, and that of K-feldspar would produce negative Eu–Ba anomalies (Hanson, 1978). In log–log diagrams of Ba *vs* Sr and Ba/Sr *vs* Sr (Fig. 12), the Sr and Ba concentrations of the Zhengga biotite granites decrease moderately in the early stage of crystallisation but decrease sharply in the later stages. These could be explained by the early fractionation of plagioclase, followed by the later fractionation of K-feldspar and plagioclase, rather than biotite, (Fig. 12). Details of the fractional crystallisation modelling are given in Supplementary Data File 7. Plagioclase crystals from the biotite granites show oscillatory compositional zoning with a decreasing An (anorthite) component from andesine cores to oligoclase mantles and rims (Figs 3 and 4). These complex zoning patterns are most likely related to long-lived magma recharge and fractionation. The early crystals have undergone resorption and overgrowth in later more evolved magma.

Calculation of zircon saturation temperatures (T_{Zr}) using the updated equation proposed by Boehnke *et al.* (2013) yield 629 ˚C to 660 ˚C (Table 2). A study of granites from Cordillera in the United States and New Zealand indicate that their zircon saturation temperatures (T_{Zr}) are universally lower (<800 °C) than those expected from dehydration melting of mafic crust (T >900 °C) (Collins *et al.*, 2016). Accordingly Collins *et al.* (2016) proposed that silicic Cordilleran magmas form in magmatic arcs where hydrous basaltic magmas solidify in the arc root, producing a mafic underplate that emits aqueous fluids which transfer to the crust and promote water-fluxed partial melting at ambient temperature and pressure (~750–800 °C at 8 kbar) conditions. In addition, low Zr (53–76 ppm) contents and lack of inherited zircon grains in the Zhengga biotite granites are consistent with significant fractional crystallization of zircon or a source undersaturated in zircon (Table 2 and Supplementary Data File 4). These inheritance-poor granitoids are undersaturated in zircon and hence the calculated T_{Zr} (< 800 ˚C) is likely to reflect the minimum emplacement temperature, which is lower than initial generation temperature (Miller *et al.*, 2003). Thus, we use alkali feldspar ($An_{0–4}Ab_{12–42}Or_{58–85}$) and andesine ($An_{30–48}Ab_{51–69}Or_{0–2}$) as combinations of early feldspars to estimate the formation temperature of the Zhengga biotite granites. Calculations using the two-feldspar (plagioclase and alkali feldspar) thermometer of Putirka *et al.* (2008) indicate that the Zhengga biotite granites have high initial formation temperatures of 889–998 °C, which is consistent with coeval high-T (> 800 °C) granulite facies metamorphism in the Eastern Himalayan Syntaxis (Guo *et al.*, 2012; Zhang *et al.*, 2013).

Mineral assemblages in the crustal source of the felsic rocks can be further constrained by their geochemical characteristics. Given that plagioclase is enriched in Sr, and garnet is depleted in LREE and enriched in HREE and Y, the moderately

negative to positive Sr (Sr*/Sr = 0.7–1.4) anomalies (Fig. 8b), and low La/Yb and Sr/Y ratios of the Zhengga biotite granites (Fig. 13a; Table 2), reflect a plagioclase-rich source containing little or no garnet (Rapp & Watson, 1995; Qian & Hermann, 2013). Pressure–temperature conditions for partial melting of crustal rocks based on experimental data are summarized in Fig. 13b. They indicate that garnet forms at pressures of 0.4–0.6 GPa and temperatures of 750–900 °C during partial melting of metasedimentary rocks (Clemens & Wall, 1981; Steven *et al*., 1997; Patiño Douce & Harris, 1998; Wang *et al*., 2012), and that the lower limit of garnet stability is 0.5 GPa (Line 9 in Fig. 13b). Plagioclase is a common residual mineral during partial melting of metasedimentary and igneous rocks (such as tonalites and basalts), but it disappears at pressures > 1.2–1.5 GPa (Rapp & Watson, 1995; Rapp *et al*., 2003; Patiño Douce, 2005; Xiong *et al*., 2005) (Fig. 13b). Thus, these features suggest that the formation of the Zhengga biotite granites occurred over a range of pressures from 0.5–1.2 GPa, consistent with magmatic epidote from the Zhengga gabbros (Ma *et al*., 2013b). In addition, most of the Paleocene magmatic rocks are also characterised by low La/Yb and Sr/Y ratios relative to the latest Cretaceous granites (Fig. 13a), suggesting a relatively thin crust in the southern Lhasa Block during the Paleocene, which is also supported by previous work (Ji *et al*., 2014).

In summary, all these features support a model in which the Zhengga biotite granites were generated by high degrees of partial melting (10% to 50%) of Gangdese juvenile middle-lower crust with minor (~5%) ancient Lhasa crustal basement (represented by two-mica granite) in the temperature range 889–998 °C. These melts subsequently underwent magma recharge and fractional crystallisation of K-feldspar and plagioclase in deep (15–40 km) crustal magma chambers.

Garnet-bearing two-mica granites

Most leucogranites are characterised by high silica and alumina, and usually contain aluminium-bearing minerals, such as garnet, tourmaline, muscovite and cordierite (Le Fort, 1975). Thus, leucogranite is recognized as being a typical product of partial melting of metasediments (e.g., Le Fort, 1981; Patiño Douce & Harris, 1998; Harrison *et al*., 1999; Searle *et al*., 2010; Guo & Wilson, 2012). This model is supported by Cenozoic Himalayan leucogranites that are characterised by high silica contents (> 70 wt %), low TiO_2, MgO and total Fe_2O_3 (< 1 wt %) contents, peraluminous compositions (A/CNK > 1.1), high initial $^{87}Sr/^{86}Sr$ ratios of 0.73–0.78; and low $\varepsilon_{Nd}(t)$ values of −10 to −15. It has been proposed that these granites are derived from the metapelites of the High Himalayan Crystalline Sequence (e.g., Inger & Harris, 1993; Harrison *et al*., 1999; Murphy, 2007; King *et al*., 2011; Guo & Wlison, 2012).

The Paleocene Zhengga garnet-bearing, two-mica granites are characterised by relatively depleted Sr-Nd isotopic composition ($\varepsilon_{Nd}(t)$ = +0.43 to +0.77; $(^{87}Sr/^{86}Sr)_i$ = 0.7037 to 0.7050), which clearly distinguish them from the Devonian ancient crust-derived granites and the Miocene High Himalayan leucogranites (Fig. 9a). In addition, the Paleocene Zhengga garnet-bearing, two-mica granites have relatively low $\delta^{18}O$ values (5.5–7.3‰) similar to the Zhengga biotite granites and gabbros (Fig. 9d; Supplementary Data File 5), that are inconsistent with a metasedimentary source. High $\varepsilon_{Hf}(t)$ (+5.5–+11.7) values of the garnet-bearing granite sample 09TB66 also support this inference (Supplementary Data File 5). These features, combined with the nearly identical Sr and Nd isotopic compositions (Fig. 9a) of the garnet-bearing, two-mica granites and the coeval biotite granites, indicate they are likely to be derived from a similar source.

Compared to the biotite granites, the Zhengga garnet-bearing granites have higher

silica contents (72.7–75.6 wt %; Fig. 7a), markedly lower concentrations of other major oxides (such as TiO_2, MgO, $Fe_2O_3^T$ and CaO), and display marked depletions in Ba, Sr, Ti and Eu (Sr/Sr* = 0.17–0.34; Ti/Ti* = 0.02–0.06; Eu/Eu* = 0.08–0.16; Table 2), suggesting that they have experienced significant fractionation. The biotite and muscovite in the garnet-bearing granites also both have low TiO_2 contents (0.04–1.21 wt % and 0.03–0.14 wt %, respectively) (Supplementary Data File 3), that further support extensive fractionation. Plagioclase from the garnet-bearing granites consists of a core of oligoclase ($An_{13-21}Ab_{78-86}Or_1$) and rim of albite ($An_{6-9}Ab_{90-93}Or_{1-2}$) (Fig. 4) and has mostly lower An (anorthite) contents compared to the biotite granites, also suggesting a more evolved magma.

Negative Ti anomalies indicate fractionation of Ti-bearing phases (e.g., titanite, ilmenite and rutile). Extensive fractionation of K-feldspar with minor plagioclase is responsible for marked Eu depletion in these rocks (Fig. 8). Given that biotite crystallisation in peraluminous magmas is favoured by elevated Fe, Mg and Ti contents (Scaillet *et al*., 1995), the low Fe and Mg contents are interpreted to result from fractionation of biotite and amphibole. Zircon and apatite both have high partition coefficients for the REE, whereas garnet has very low partition coefficients for the light REE and large partition coefficients for the heavy REE. In previous studies it has been proposed that REE contents are mainly controlled by accessory minerals such as zircon, apatite, allanite and monazite (e.g., Wu *et al*., 2003; Chu *et al*., 2009). However, given the insignificant depletion of the heavy REE (Fig. 8a) in these rocks, we contend that these accessory minerals were not significant fractionating phases during the generation of the Zhengga garnet-bearing granites.

The Zhengga garnet-bearing, two-mica granites are characterised by abundant almandine-rich garnet and muscovite and are different from the biotite granites (Fig. 2;

Table1; Supplementary Data File 3). Previous experimental work has proposed two main models for the origin of garnet in peraluminous granitoids:

1) Muscovite + Biotite + 3Quartz = Garnet + 2K-feldspar + $2H_2O$ (e.g., Abbott & Clarke, 1979; Clemens & Wall, 1981);

2) Biotite + (Mn, Al)-rich liquid = Garnet + Muscovite (Miller & Stoddard, 1981).

Given the presence of garnet and muscovite (Table1) and the decreasing abundance of biotite, we propose that the second model best explains the formation of garnet and muscovite in the Zhengga garnet-bearing two-mica granites. Plagioclase (mostly albite) in the garnet-bearing granites has lower An and higher Al_2O_3 contents compared to the biotite granites (Supplementary Data File 3) and all magmatic garnets show spessartine-enrichment ($Alm_{23-59}Sps_{36-64}Pyr_{1-5}And_{0-8}$; MnO = 12.5–27.4 wt %; Supplementary Data File 3), consistent with an evolved (Mn, Al)-rich liquid that supports model 2 for the formation of garnet and muscovite.

Garnets from the Zhengga garnet-bearing granites have low pyrope and relatively high almandine and spessartine contents (Supplementary Data File 3). Pyrope-rich garnet generally coexists with high temperature (>950 °C) melts (Green, 1977). Thus, the presence of pyrope-poor garnet in the garnet-bearing granites suggests relatively low temperatures (<950 °C), consistent with low zircon saturation temperatures (598–661 °C; Table 2). Nevertheless, given relatively low Zr contents and negative Zr anomalies (Fig. 8b; Table 2), suggesting significant fractionation of zircon and undersaturation in Zr, the zircon saturation temperatures are likely to be underestimated (by up to +50 °C) (Miller *et al*., 2003).

It has been proposed that Mn-enrichment enhances the stability of garnet in magmas (Green, 1977; Clemens & Wall, 1981; Miller & Stoddard, 1981). The MnO and CaO contents of experimentally crystallized garnets show an antithetic

relationship (Green, 1977), consistent with garnets in the Zhengga garnet-bearing granites (Fig. 5; Supplementary Data File 3). The grossular content of crystallizing garnets increases with increasing pressure (Green, 1977). Thus, the low grossular and high spessartine contents of the garnet suggest that the Zhengga garnet-bearing, two-mica granites were formed at relatively low pressure. Experimental data indicate that almandine-rich garnet is most stable in silicic melts with 3–5 wt % water at T <850°C and P >4–5 kbar (e.g., Clemens & Wall, 1981). Moreover, spessartine-rich garnets could be stable in silicic magmas to pressures as low as 3 kbar (Green, 1977). The magmatic garnets in the garnet-bearing, two-mica granites exhibit similar compositional zoning (i.e., $Alm_{54\text{-}59}Sps_{36\text{-}51}$) and are characterised by increasing Mn, decreasing Fe and oscillatory Ca from core to rim, with a narrow outermost rim that is richest in Mn (Fig. 5). These compositional features are most likely the result of crystallization from a highly evolved magma (Clemens & Wall, 1981) and, or, at low pressure (Green, 1977).

In summary, the garnet-bearing, two-mica granites are likely to represent the products of advanced fractionation of the biotite-granite magmas at relatively high temperature (~650–700 °C) in magma chambers at mid-crust depths (~12–18 km) during the latest stage of magma evolution. Their compositional features can be explained by fractionation of K-feldspar, biotite and titanite with minor plagioclase and accessory minerals, such as zircon, apatite, allanite and monazite. Garnet and muscovite were most likely formed by reaction between biotite and highly evolved (Mn, Al)-rich melt.

Paleocene magmatism and diachronous continental collision

The distribution of Paleocene magmatism within the Lhasa Block of South Tibet is

summarized in Supplementary Data File 1. An early Paleocene linear magmatic and metamorphic belt stretches for over 1500 kilometres to the north of the Indus–Yarlung Tsangpo suture; this comprises an eastern segment from Xigaze to Nyingchi (between 95°E to 86ºE) (Fig. 1b) and a western segment (between 82°E to 80ºE) with a quiescent magmatic area in the central Gangdese (between 86°E to 82ºE) (Supplementary Data File 1). Given the Paleocene magmatism and coeval magmatic quiet/quiescent area in the central Gangdese, we advocate a diachronous continent-continent collision model in which India collided first with the middle part of southern Tibet at ~65–63 Ma, followed by suturing progressing both westward and eastward at ~55–50 Ma (Fig. 14).

In the early Paleocene (~65–63 Ma), the northernmost part of the Greater Indian continent first collided with the Asian continent in central Lhasa (approximately between 86°E to 82ºE; Fig. 14). The resistance generated by this initial collision event between the Indian and Asian continents and buoyancy forces due to the lower density of the continental crust are likely to have resulted in a change in subduction velocity and angle (Buck & Toksöz, 1983; Shellnutt *et al*., 2014). This change in subduction velocity is consistent with the abrupt deceleration of the convergence rate between India and Asia from 170 to 100 mm/yr at ~60 Ma (e.g., Lee & Lawver, 1995). Collision led to crustal thickening and cessation of central Gangdese magmatism (Zhu *et al*., 2017). An initial collision event between Asian and Indian continental crustal blocks in the Early Paleocene (ca. 65–63 Ma) is also supported by:

1) Hf isotope and geochronological data of detrital zircons from the Sangdanlin and Gyangze basins, located along the southern flank of the Indus-Yarlung suture zone. These data suggest that Asian-derived clastic sediments started contributing to sedimentation on the Indian continental margin at ~60 Ma (DeCelles *et al*., 2014; Wu

et al., 2014), hence there was direct contact between the continental blocks at this time;

2) Provenance analysis for upper Cretaceous strata in the Gyangze, Zhepure Mountain and Sangdanlin section of the Tethyan-Himalaya indicates that the collision of India with Asia occurred before ca. 65–60 Ma (Cai *et al*., 2011; Hu *et al*., 2015; DeCelles *et al*., 2014);

3) The oceanic rocks in ophiolite mélanges were obducted onto the northern margin of India during latest Cretaceous–earliest Tertiary time (ca. 66–62) (Ding *et al*., 2005);

4) A paleomagnetic study of Paleocene marine sediments in the Gamba area of the Tethyan Himalaya in southern Tibet further constrains the timing of initial contact between India and Asia to before 60.5±1.5 Ma (Yi *et al*., 2011).

Hu *et al*. (2017) defined diachronous collision as when the initial timings of two distant collision events on the same margin are more than 5 Ma apart. Thus, the following evidence for a later (ca. 55–50 Ma) collision in the eastern and western Gangdese further support the diachronous collision model:

1) Metamorphism of the subducted leading edge of the Indian continent (Tso Morari eclogite) and syn-collisional adakites in Ladakh of the western Himalaya took place at ~ 53 to 47 Ma (Leech *et al*., 2005, 2007; Shellnutt *et al*., 2014);

2) A provenance study of the youngest detrital sedimentary rocks in the western Tethyan Himalaya of the Indian plate show that zircons of Asian affinity were deposited on the Indian plate at 54 Ma and constrain terminal India–Asia collision to have occurred in the Western Himalaya by 54 Ma (Najman *et al*., 2017);

3) Detrital zircon geochronology for the Cenozoic foreland basin strata in the Hazara–Kashmir syntaxial region of northern Pakistan indicates that a provenance

shift from Indian affinity to Asian affinity occurred at ca. 56–55 Ma (Ding *et al.*, 2016b);

4) Work on collision-related medium-pressure metamorphism in the eastern Himalayan Yardoi area of eastern Tibet suggests that the onset of the Asia-India collision had occurred by ~50 Ma (Ding *et al.*, 2016a).

Paleocene crustal anatexis and soft collision in southern Lhasa

We show in our study that the Paleocene (ca. 63–57 Ma) Zhengga garnet-bearing, two-mica granites and biotite granites in the Gangdese batholith probably originated from a middle-lower crustal source, including juvenile and ancient materials. Existing data suggest the existence of a Paleocene crustal magmatic belt along the southern flank of the Indus-Yarlung suture zone (Fig. 1b). This Paleocene magmatism consists of adakites, I- and S-type granites and minor gabbros and rhyolites and ignimbrites from the Dianzhong Formation; these have positive and negative $\varepsilon_{Nd}(t)$ and zircon $\varepsilon_{Hf}(t)$ values (Fig. 9), which indicate that most Paleocene granites in southern Lhasa were derived from the partial melting of crustal rocks (e.g., Guo *et al.*, 2012; Lee *et al.* 2012; Zhang *et al.*, 2013; Jiang *et al.*, 2014; Wang *et al.*, 2015; Zhu *et al.*, 2015). Therefore, a significant crustal anatexis event is proposed to have occurred during the Paleocene (ca. 63–57 Ma) in the Xigaze–Nyingchi area of the southern Lhasa sub-block (Fig. 1b).

Metamorphic phase equilibrium modelling shows that the pelitic schists from the Nyingchi complex in the eastern Gangdese underwent significant near-isobaric cooling in the granulite-facies field at high temperature of 700–830°C and nearly constant pressure of 10–11 kbar (Zhang *et al.*, 2013). Our temperature calculations using the two-feldspar thermometer (Putirka *et al.*, 2008) also suggest that the

Zhengga biotite granites with low La/Yb and Sr/Y ratios were derived from a mid-lower crustal source at high temperatures of 889 to 998 °C. Similar Sr-Nd and zircon O isotope variations (Fig. 9) with increasing SiO_2 and decreasing Mg, Fe and Ti contents (Table 2) from the Zhengga biotite granites to garnet-bearing two-mica granites indicate they were products of different evolutionary stages in mid-lower crustal magma chambers during magma ascent and emplacement (Fig. 14). The compositional zoning of feldspar and garnet (Figs 4–6) and variable Ti contents of biotite (Supplementary Data File 3) also indicate that the Paleocene Zhengga granites have undergone magma recharge and fractionation at temperatures and pressures of ~650–800 °C and 1.2–0.4 GPa, respectively. Thus, high-temperature mid-lower crustal magma chambers likely were widespread in southern Lhasa and also could explain the presence of coeval high temperature syn-intrusion granulite rocks in the south Lhasa Block (Guo *et al*., 2012; Zhang *et al*., 2013) (Fig. 14).

In this study, plagioclase crystals from the Zhengga granites showing a broad range of compositions from andesine ($An_{30-48}Ab_{51-69}Or_{1-11}$) to albite ($An_{1-3}Ab_{97-98}Or_1$) (Fig. 4; Supplementary Data File 3) require a long-lived (>1 Myr) magma chamber (Karakas *et al*., 2017). However, sustaining such a long-term chamber is not easy. Numerical models indicate that an initial magma body is usually small and prone to frequent eruptions upon recharge and also undergoes rapid (less than 10^5 yr) cooling in a cold host crust (Degruyter & Huber, 2014; Karakas *et al*., 2017). As a consequence the chamber will likely crystallize and become mechanically locked before it can grow by any appreciable amount. Both temperature and pressure decrease as a function of time (Liang, 2017). Thus, a low decompression rate, low cooling rate and high mass inflow rate could all potentially explain the growth of large silicic reservoirs in the shallow crust (Degruyter & Huber, 2014; Karakas *et al*.,

2017; Liang, 2017).

As discussed above, a significant amount of evidence supports an initial Paleocene onset of continental collision. However, the convergence between two cold continents seems incompatible with the large-scale magmatism in the southern Lhasa terrane between ca. 65–45 Ma (e.g., Chung *et al*., 2005; Wen *et al*., 2008; Ji *et al*., 2009; Lee *et al*., 2009, 2012; Zhu *et al*., 2015, 2017), which is also the main reason why magmatism cannot accurately constrain the timing of initial collision. Here, we propose a model of interaction between initial continental collision and oceanic slab roll-back to account for the above observations and other Paleocene geological features in the region (Fig. 14).

A slab roll-back model has been widely proposed to explain early Paleocene crustal anatexis and metamorphism in southern Lhasa (e.g., Chung *et al*., 2005; Kapp *et al*., 2005, 2007; Wen *et al*., 2008; Lee *et al*., 2009, 2012; Guo *et al*., 2012; Zhang *et al*., 2013; Zhu *et al*., 2013, 2017). Generally, slab roll-back triggers mantle corner flow and asthenospheric upwelling and results in significant partial melting of sub-continental lithospheric mantle and lower crust, similar to that proposed for the Late Cretaceous southern Lhasa terrane (Ma *et al*., 2013a, 2015) and the Eocene Ladakh Batholith (Shellnutt *et al*., 2014). Here, we propose that the initial collision in central Lhasa followed slab roll-back and resulted in cessation of central Gangdese magmatism and crustal thickening. Despite this, the early Paleocene crustal thickening was probably limited but the crustal thickening triggered by continental convergence likely suppressed decompression partial melting of sub-continental lithospheric mantle and generated a thermal boundary between crust and lithospheric mantle beneath southern Lhasa (Buck & Toksöz, 1983). Future work on Paleocene primitive mantle-derived rocks and lower crust-derived adakites in the region will

yield more information on crustal thickness and the thermal state of the lithosphere and may provide a test for the validity of this inference.

A sudden rise in convergence rate is identified prior to initial collision (Lee & Lawver, 1995; White & Lister, 2012), which likely correlates with roll-back of the Neo-Tethyan slab (Chung *et al*., 2005; Shellnutt *et al*., 2014). The roll-back would facilitate the dragging down of the attached Indian continental lithosphere to greater depths (Chemenda *et al*., 2000). This process explains why there was a general lack of contraction and shortening at upper crustal levels along the Gangdese arc and elsewhere in the Lhasa Block in the Paleogene (e.g., Chung *et al*., 2005 and references therein).

Subsequently, the resistance generated by the initial Indo-Asian collision and buoyancy forces due to the lower density of the continental crust were likely to result in the abrupt deceleration of the convergence rate between India and Asia from 170 to 100 mm/yr at ~60 Ma (e.g., Lee & Lawver, 1995). Slab roll-back may have continued as suturing progressed (von Blanckenburg & Davies, 1995). It would have been accompanied by a southward migration of asthenospheric convection beneath Tibet, which would have significantly enhanced the asthenospheric corner flow and changed the thermal structure of the mantle wedge (Chung *et al*., 2005). This process would supply a long-lived heat source for crustal anatexis by thermal diffusion. Moreover, increased pressure and crustal thickening resulting from progression of suturing and a reduced crustal cooling rate would have extended the lifetime of crustal magma reservoirs in southern Lhasa (Fig. 14).

Mid-lower crustal flow has been widely recognized on a large scale in the Tibet-Himalaya Orogen and has played a role in crustal processes and thermal structure, such as melting, thinning, surface deformation and exchange or

transportation of material (e.g., Nelson *et al*., 1996; Royden *et al*., 1997; Beaumont *et al*., 2001; Shapiro *et al*., 2004; King *et al*., 2011). Rosenberg & Handy (2005) proposed a melt fraction of > 7 vol.% as the 'melt connectivity transition', marking an increase of melt interconnectivity that causes a dramatic drop in crustal strength. Our melt modelling suggests that the Paleocene Zhengga biotite granites were formed by high degrees (10–50 vol.%) of partial melting at 889–998°C (Fig. 12). This, combined with the extensive crustal anatexis in the western and eastern Gangdese, as discussed above, supports the likelihood of crustal flow in southern Tibet, similar that which occurred in central and northern Tibet example (Wang *et al*., 2016). Further support for this model has been provided by Wu *et al*. (2017), who have recently proposed that granitic differentiation is dominated by flow segregation or dynamic sorting rather than crystal settling by gravitation. Thus, the Zhengga highly evolved garnet-bearing two-mica granites may also have experienced crustal flow, which would have contributed to crustal thickening (Zhu *et al*., 2017) (Fig. 14). An abrupt Paleogene shift in zircon Hf isotope compositions in Triassic–Eocene Gangdese granitoids and post-collisional adakites from Mesozoic depleted mantle-type signatures to more enriched crustal characteristics, prior to formation of subducted Indian crust-derived adakites, potentially reveal a hidden input from Indian continental crust (Chu *et al*., 2011). Middle-low crustal flow would provide an effective mechanism to supply an input from Indian crust before the full contact between Indian-Asian continents.

Widespread high-temperature crustal anatexis and metamorphism resulted in hot and weakened crust in southern Lhasa. In addition, three-dimensional models indicate that slab roll-back is likely accompanied by trench migration (Stegman *et al*., 2006). Both the trench retreat and coeval Lhasa crustal anatexis would buffer the impact

from the India continent, which is congruous with a soft collision in the Early Paleocene as advocated by Lee & Lawver (1995) and Chung *et al.* (2005). This large-scale interaction between continental collision and oceanic subduction not only has the potential to explain the evolution of the Paleocene Himalayan-Tibetan orogeny, but it could also help explain the anomalously hot lithosphere and crust in some other large-scale convergence zones on Earth (Buck & Toksöz, 1983).

CONCLUSIONS

1. Garnet-bearing two-mica granites and associated biotite granites in the Sangri area, southern Tibet, were emplaced in the Paleocene (ca. 63–57 Ma).

2. The Zhengga biotite granites were generated by high degree (10% to 50%) partial melting of a mid-lower crustal source comprising Gangdese juvenile crust with minor (~5%) ancient Lhasa crust at high temperatures of 889–998 °C.

3. The Zhengga garnet-bearing two-mica granites appear to be derived from advanced fractionation of biotite-granite magmas in relatively high temperature (~700–750 °C) magma chambers at mid-crust depths (~12–18 km).

4. A Paleocene magmatic and high temperature metamorphic belt, extending linearly for more than 1500 km along the north of the Indus–Tsangpo Suture, suggests that a significant Early Paleocene crustal anatectic event occurred in the Xigaze–Nyingchi area of the southern Lhasa sub-block.

5. The interaction between continental collision and subducted slab roll-back may be responsible for the evolution of the Paleocene Himalayan-Tibetan orogeny; similar processes may have occurred in other large-scale convergence zones.

ACKNOWLEDGEMENTS

We are very grateful for the hard work of Georg Zellmer, Greg Shellnutt, Romain Tartèse, Mei-Fei Chu and another reviewer, whose constructive criticism and suggestions have led to clarification of various aspects of this paper. We appreciate the assistance of Yong–Sheng Liu, Yue–Heng Yang, Zhao–Chu Hu, Xi-Rong Liang, Xiang–Lin Tu, Jin–Long Ma, Qing Yang, Chang-ming Xing, Lie–Wen Xie, Wan-Feng Zhang, Bo-Qin Xiong, Guang–Qian Hu and Ying Liu for zircon age, whole-rock and mineral geochemical analyses.

FUNDING

Financial support for this research was provided by the DREAM Programs of China (2016YFC0600309 and 2016YFC0600407), the Strategic Priority Research Program (B) of the Chinese Academy of Sciences (XDB03010600), the National Natural Science Foundation of China (Nos. 41402048, 41630208, and 41421062), talent project of Guangdong Province (2014TX01Z079), the Key Program of the Chinese Academy of Sciences (QYZDJ-SSW-DQC026), the State Scholarship Fund of China (No. 201604910124) and the Guangzhou Institute of Geochemistry, Chinese Academy of Sciences (GIGCAS 135 project 135TP201601). This is contribution No. IS-XXXX from GIGCAS.

SUPPLEMENTARY DATA

Supplementary data for this paper are available at http://*****

REFERENCES

Abbott, R. & Clarke, D. B. (1979). Hypothetical liquidus relationships in the subsystem Al_2O_3-FeO-MgO projected from quartz, alkali feldspar and plagioclase for a (H_2O)< or= 1. Canadian Mineralogist 17, 549-560.

Allégre, C., Courtillot, V., Tapponnier, P., Hirn, A., Mattauer, M., Coulon, C., Jaeger, J., Achache, J., Schärer, U. & Marcoux, J. (1984). Structure and evolution of the Himalaya–Tibet orogenic belt. Nature 307, 17-22.

Beaumont, C., Jamieson, R. A., Nguyen, M. & Lee, B. (2001). Himalayan tectonics explained by extrusion of a low-viscosity crustal channel coupled to focused surface denudation. Nature 414, 738-742.

Beck, R. A., Burbank, D. W., Barndt, J. K., Berryf, J. R., Afzal, J., Khan, A. M., Jurgen, H., Metje, J., Cheema, A. & Shafique, N. A. (1995). Stratigraphic evidence for an early collision between. Nature 373, 5.

Boehnke, P., Watson, E. B., Trail, D., Harrison, T. M. & Schmitt, A. K. (2013). Zircon saturation re-revisited. Chemical Geology 351, 324-334.

Brown, M. (2007). Crustal melting and melt extraction, ascent and emplacement in orogens: mechanisms and consequences. Journal of the Geological Society 164, 709-730.

Buck, W. R. & Toksöz, M. N. (1983). Thermal effects of continental collisions: Thickening a variable viscosity lithosphere. Tectonophysics 100, 53-69.

Cai, F., Ding, L. & Yue, Y. (2011). Provenance analysis of upper Cretaceous strata in the Tethys Himalaya, southern Tibet: Implications for timing of India–Asia collision. Earth and Planetary Science Letters 305, 195-206.

Chappell, B. & White, A. (1992). I-and S-type granites in the Lachlan Fold Belt. Geological Society of America Special Papers 272, 1-26.

Chemenda, A. I., Burg, J.-P. & Mattauer, M. (2000). Evolutionary model of the Himalaya–Tibet system: geopoem: based on new modelling, geological and geophysical data. Earth and Planetary Science Letters 174, 397-409.

Chu, M. F., Chung, S. L., Song, B., Liu, D., O'Reilly, S. Y., Pearson, N. J., Ji, J. & Wen, D. J. (2006). Zircon U-Pb and Hf isotope constraints on the Mesozoic tectonics and crustal evolution of southern Tibet. Geology 34, 745-748.

Chu, M.-F., Chung, S.-L., O'Reilly, S. Y., Pearson, N. J., Wu, F.-Y., Li, X.-H., Liu, D., Ji, J., Chu, C.-H. & Lee, H.-Y. (2011). India's hidden inputs to Tibetan orogeny revealed by Hf isotopes of Transhimalayan zircons and host rocks. Earth and Planetary Science Letters 307, 479-486.

Chu, M.-F., Wang, K.-L., Griffin, W. L., Chung, S.-L., O'Reilly, S. Y., Pearson, N. J. & Iizuka, Y. (2009). Apatite Composition: Tracing Petrogenetic Processes in Transhimalayan Granitoids. Journal of Petrology 50, 1829-1855.

Chung, S.-L., Chu, M.-F., Zhang, Y., Xie, Y., Lo, C.-H., Lee, T.-Y., Lan, C.-Y., Li, X., Zhang, Q. & Wang, Y. (2005). Tibetan tectonic evolution inferred from spatial and temporal variations in post-collisional magmatism. Earth-Science Reviews 68, 173-196.

Clemens, J. D. & Wall, F. (1981). Origin and crystallization of some peraluminous (S-type) granitic magmas. Canadian Mineralogist 19, 111-131.

Coleman, M. E. (1998). U-Pb constraints on Oligocene-Miocene deformation and anatexis within the central Himalaya, Marsyandi Valley, Nepal. American Journal of Science 298, 553-571.

Collins, W. J., Huang, H.-Q. & Jiang, X. (2016). Water-fluxed crustal melting produces Cordilleran batholiths. Geology 44, 143-146.

Coulon, C., Maluski, H., Bollinger, C. & Wang, S. (1986). Mesozoic and Cenozoic volcanic rocks from central and southern Tibet: ^{39}Ar-^{40}Ar dating, petrological characteristics and geodynamical significance. Earth and Planetary Science Letters 79, 281-302.

Decelles, P. G., Kapp, P., Gehrels, G. E. & Ding, L. (2014). Paleocene - Eocene foreland basin evolution in the Himalaya of southern Tibet and Nepal: Implications for the age of initial India - Asia collision. Tectonics 33, 824-849.

Degruyter, W. & Huber, C. (2014). A model for eruption frequency of upper crustal silicic magma chambers. Earth and Planetary Science Letters 403, 117-130.

Dewey, J. F., Shackleton, R. M., Chengfa, C. & Yiyin, S. (1988). The tectonic evolution of the Tibetan Plateau. Philosophical Transactions of the Royal Society of London. Series A, Mathematical and Physical Sciences 327, 379-413.

Ding, L., Kapp, P. & Wan, X. (2005). Paleocene-Eocene record of ophiolite obduction and initial India-Asia collision, south central Tibet. Tectonics 24, 1-18.
Ding, H., Zhang, Z., Dong, X., Tian, Z., Xiang, H., Mu, H., Gou, Z., Shui, X., Li, W. & Mao, L., (2016a). Early Eocene (c. 50 Ma) collision of the Indian and Asian continents: Constraints from the North Himalayan metamorphic rocks, southeastern Tibet: Earth and Planetary Science Letters 435, 64-73.
Ding, L., Qasim, M., Jadoon, I. A., Khan, M. A., Xu, Q., Cai, F., Wang, H., Baral, U. & Yue, Y. (2016b). The India–Asia collision in north Pakistan: Insight from the U–Pb detrital zircon provenance of Cenozoic foreland basin. Earth and Planetary Science Letters 455, 49-61.
Dong, X., Zhang, Z., Liu, F., He, Z. & Lin, Y. (2014). Late Paleozoic intrusive rocks from the southeastern Lhasa terrane, Tibetan Plateau, and their Late Mesozoic metamorphism and tectonic implications. Lithos 198, 249-262.
Eiler, J. M. (2001). Oxygen isotope variations of basaltic lavas and upper mantle rocks. Reviews in mineralogy and geochemistry 43, 319-364.
Eiler, J. M. (2007). On the origins of granites. Science 315, 951-952.
Green, T. (1977). Garnet in silicic liquids and its possible use as a PT indicator. Contributions to Mineralogy and Petrology 65, 59-67.
Guo, L., Zhang, H. F., Harris, N., Parrish, R., Xu, W. C. & Shi, Z. L. (2012). Paleogene crustal anatexis and metamorphism in Lhasa terrane, eastern Himalayan syntaxis: Evidence from U-Pb zircon ages and Hf isotopic compositions of the Nyingchi Complex. Gondwana Research 21, 100-111.
Guo, Z. & Wilson, M. (2012). The Himalayan leucogranites: constraints on the nature of their crustal source region and geodynamic setting. Gondwana Research 22, 360-376.
Hacker, B. R., Ritzwoller, M. H. & Xie, J. (2014). Central Tibet has a partially melted, mica-bearing crust. Tectonics 33, 1408–1424.
Hanson, G. N. (1978). The application of trace elements to the petrogenesis of igneous rocks of granitic composition. Earth and Planetary Science Letters 38, 26-43.
Harrison, M. T., Grove, M., Mckeegan, K. D., Coath, C., Lovera, O. M. & Le Fort, P. (1999). Origin and episodic emplacement of the Manaslu intrusive complex, central Himalaya. Journal of Petrology 40, 3-19.
Harrison, T. M., Lovera, O. M. & Grove, M. (1997). New insights into the origin of two contrasting Himalayan granite belts. Geology 25, 899-902.
Hawkesworth, C., Turner, S., McDermott, F., Peate, D. & Van Calsteren, P. (1997). U-Th isotopes in arc magmas: Implications for element transfer from the subducted crust. science 276, 551-555.
Hoskin, P. & Black, L. (2000). Metamorphic zircon formation by solid state recrystallization of protolith igneous zircon. Journal of Metamorphic Geology 18, 423-439.
Hu, X., Garzanti, E., Moore, T. & Raffi, I. (2015). Direct stratigraphic dating of India-Asia collision onset at the Selandian (middle Paleocene, 59±1 Ma). Geology 43, 859-862.
Hu, X., Wang, J., An, W., Garzanti, E. & Li, J. (2017). Constraining the timing of the India-Asia continental collision by the sedimentary record. Science China Earth Sciences 60, 603-625.
Inger, S. & Harris, N. (1993). Geochemical constraints on leucogranite magmatism in the Langtang Valley, Nepal Himalaya. Journal of Petrology 34, 345-368.
Ji, W.-Q., Wu, F.-Y., Chung, S.-L. & Liu, C.-Z. (2012). Identification of Early Carboniferous Granitoids from Southern Tibet and Implications for Terrane Assembly Related to the Paleo-Tethyan Evolution. The Journal of geology 120, 531-541.
Ji, W. Q., Wu, F. Y., Chung, S. L., Li, J. X. & Liu, C. Z. (2009). Zircon U-Pb geochronology and Hf isotopic constraints on petrogenesis of the Gangdese batholith, southern Tibet. Chemical Geology 262, 229-245.
Ji, W.-Q., Wu, F.-Y., Chung, S.-L. & Liu, C.-Z. (2014). The Gangdese magmatic constraints on a latest Cretaceous lithospheric delamination of the Lhasa terrane, southern Tibet. Lithos 210, 168-180.
Jiang, Z.-Q., Wang, Q., Wyman, D. A., Li, Z.-X., Yang, J.-H., Shi, X.-B., Ma, L., Tang, G.-J., Gou, G.-N. & Jia, X.-H. (2014). Transition from oceanic to continental lithosphere subduction in southern Tibet: Evidence from the Late Cretaceous–Early Oligocene (~ 91–30Ma) intrusive rocks in the Chanang–Zedong area, southern Gangdese. Lithos 196, 213-231.

Kapp, P., DeCelles, P. G., Gehrels, G. E., Heizler, M. & Ding, L. (2007). Geological records of the Lhasa-Qiangtang and Indo-Asian collisions in the Nima area of central Tibet. Geological Society of America Bulletin 119, 917-932.

Kapp, P., Yin, A., Harrison, T. M. & Ding, L. (2005). Cretaceous-Tertiary shortening, basin development, and volcanism in central Tibet. Geological Society of America Bulletin 117, 865-878.

Karakas, O., Degruyter, W., Bachmann, O. & Dufek, J. (2017). Lifetime and size of shallow magma bodies controlled by crustal-scale magmatism. Nature Geoscience 10, 446-450.

Kemp, A., Hawkesworth, C., Foster, G., Paterson, B., Woodhead, J., Hergt, J., Gray, C. & Whitehouse, M. (2007). Magmatic and crustal differentiation history of granitic rocks from Hf-O isotopes in zircon. Science 315, 980-983.

King, J., Harris, N., Argles, T., Parrish, R. & Zhang, H. (2011). Contribution of crustal anatexis to the tectonic evolution of Indian crust beneath southern Tibet. Geological society of America bulletin 123, 218-239.

Klootwijk, C. T., Gee, J. S., Peirce, J. W., Smith, G. M. & McFadden, P. L. (1992). An early India-Asia contact: Paleomagnetic constraints from Ninetyeast Ridge, ODP Leg 121. Geology 20, 395-398.

Le Fort, P. (1975). The anatectic Himalayan leucogranites with emphasis on the Manaslu tourmaline granite. Recent researches in geology 2, 76-90.

Le Fort, P. (1981). Manaslu leucogranite: a collision signature of the Himalaya: a model for its genesis and emplacement. Journal of Geophysical Research: Solid Earth (1978–2012) 86, 10545-10568.

Le Fort, P., Cuney, M., Deniel, C., France-Lanord, C., Sheppard, S., Upreti, B. & Vidal, P. (1987). Crustal generation of the Himalayan leucogranites. Tectonophysics 134, 39-57.

Lee, H. Y., Chung, S. L., Ji, J. Q., Qian, Q., Galleta, S., Lo, C. H., Lee, T. Y. & Zhang, Q. (2012). Geochemical and Sr-Nd isotopic constraints on the genesis of the Cenozoic Linzizong volcanic successions, southern Tibet. Journal of Asian Earth Science 53, 96-114.

Lee, H.-Y., Chung, S.-L., Lo, C.-H., Ji, J., Lee, T.-Y., Qian, Q. & Zhang, Q. (2009). Eocene Neotethyan slab breakoff in southern Tibet inferred from the Linzizong volcanic record. Tectonophysics 477, 20-35.

Lee, J. & Whitehouse, M. J. (2007). Onset of mid-crustal extensional flow in southern Tibet: Evidence from U/Pb zircon ages. Geology 35, 45-48.

Lee, T. Y. & Lawver, L. A. (1995). Cenozoic plate reconstruction of Southeast Asia. Tectonophysics 251, 85-138.

Leech, M. L., Singh, S. & Jain, A. (2007). Continuous metamorphic zircon growth and interpretation of U-Pb SHRIMP dating: An example from the Western Himalaya. International Geology Review 49, 313-328.

Leech, M. L., Singh, S., Jain, A., Klemperer, S. L. & Manickavasagam, R. (2005). The onset of India–Asia continental collision: early, steep subduction required by the timing of UHP metamorphism in the western Himalaya. Earth and Planetary Science Letters 234, 83-97.

Liang, Y. (2017). Effect of pressure on closure temperature of a trace element in cooling petrological systems. Contributions to Mineralogy and Petrology 2, 1-13.

Liew, T. & Hofmann, A. (1988). Precambrian crustal components, plutonic associations, plate environment of the Hercynian Fold Belt of central Europe: indications from a Nd and Sr isotopic study. Contributions to Mineralogy and Petrology 98, 129-138.

Liu, X.-C., Wu, F.-Y., Yu, L.-J., Liu, Z.-C., Ji, W.-Q. & Wang, J.-G. (2016a). Emplacement age of leucogranite in the Kampa Dome, southern Tibet. Tectonophysics 667, 163-175.

Liu, Z.-C., Wu, F.-Y., Ding, L., Liu, X.-C., Wang, J.-G. & Ji, W.-Q. (2016b). Highly fractionated Late Eocene (~ 35Ma) leucogranite in the Xiaru Dome, Tethyan Himalaya, South Tibet. Lithos 240, 337-354.

Liu, Z.-C., Wu, F.-Y., Ji, W.-Q., Wang, J.-G. & Liu, C.-Z. (2014). Petrogenesis of the Ramba leucogranite in the Tethyan Himalaya and constraints on the channel flow model. Lithos 208, 118-136.

Ma, L., Wang, Q., Li, Z.-X., Wyman, D. A., Jiang, Z.-Q., Yang, J.-H., Gou, G.-N. & Guo, H.-F. (2013a). Early Late Cretaceous (ca. 93Ma) norites and hornblendites in the Milin area, eastern Gangdese: Lithosphere–asthenosphere interaction during slab roll-back and an insight into

early Late Cretaceous (ca. 100–80Ma) magmatic “flare-up” in southern Lhasa (Tibet). Lithos 172, 17-30.

Ma, L., Wang, Q., Wyman, D. A., Jiang, Z.-Q., Wu, F.-Y., Li, X.-H., Yang, J.-H., Gou, G.-N. & Guo, H.-F. (2015). Late Cretaceous back-arc extension and arc system evolution in the Gangdese area, southern Tibet: geochronological, petrological and Sr–Nd–Hf–O isotopic evidence from Dagze diabases. Journal of Geophysical Research: Solid Earth 120, 6159-6181.

Ma, L., Wang, Q., Wyman, D. A., Jiang, Z.-Q., Yang, J.-H., Li, Q.-L., Gou, G.-N. & Guo, H.-F. (2013b). Late Cretaceous crustal growth in the Gangdese area, southern Tibet: Petrological and Sr–Nd–Hf–O isotopic evidence from Zhengga diorite–gabbro. Chemical Geology 349, 54-70.

Miller, C. F. & Stoddard, E. F. (1981). The role of manganese in the paragenesis of magmatic garnet: an example from the Old Woman-Piute Range, California. The Journal of Geology 89, 233-246.

Miller, C. F., McDowell, S. M. & Mapes, R. W. (2003). Hot and cold granites? Implications of zircon saturation temperatures and preservation of inheritance. Geology 31, 529-532.

Mo, X. X., Zhao, Z. D., Deng, J. F., Martin, F., Yu, X. H., Luo, Z. H., Li, Y. G., Zhou, S., Dong, G. C., Zhu, D. C. & Wang, L. L. (2006). Petrology and geochemistry of postcollisional volcanic rocks from the Tibetan plateau: Implications for lithosphere heterogeneity and collision-induced asthenospheric mantle flow. Geological Society of America Special Papers 409, 507-530.

Mo, X., Hou, Z., Niu, Y., Dong, G., Qu, X., Zhao, Z. & Yang, Z. (2007). Mantle contributions to crustal thickening during continental collision: Evidence from Cenozoic igneous rocks in southern Tibet. Lithos 96, 225-242.

Murphy, M. A. (2007). Isotopic characteristics of the Gurla Mandhata metamorphic core complex: Implications for the architecture of the Himalayan orogen. Geology 35, 983-986.

Nair, R. & Chacko, T. (2008). Role of oceanic plateaus in the initiation of subduction and origin of continental crust. Geology 36, 583–586.

Najman, Y., Jenks, D., Godin, L., Boudagher-Fadel, M., Millar, I., Garzanti, E., Horstwood, M. & Bracciali, L. (2017). The Tethyan Himalayan detrital record shows that India–Asia terminal collision occurred by 54 Ma in the Western Himalaya. Earth and Planetary Science Letters 459, 301-310.

Nelson, K. D., Zhao, W., Brown, L. D., Kuo, J., Che, J., Liu, X., Klemperer, S. L., Makovsky, Y., Meissner, R., Mechie, J., Kind, R., Wenzel, F., Ni, J., Nabelek, J., Leshou, C., Tan, H., Wei, W., Jones, A. G., Booker, J., Unsworth, M., Kidd, W. S. F., Hauck, M., Alsdorf, D., Ross, A., Cogan, M., Wu, C., Sandvol, E. & Edwards, M. (1996). Partially Molten Middle Crust Beneath Southern Tibet: Synthesis of Project INDEPTH Results. Science 274, 1684-1688.

Patiño Douce, A. E. & Harris, N. (1998). Experimental constraints on Himalayan anatexis. Journal of Petrology 39, 689-710.

Patiño Douce, A. E. & Johnston, A. D. (1991). Phase equilibria and melt productivity in the pelitic system: implications for the origin of peraluminous granitoids and aluminous granulites. Contributions to Mineralogy and Petrology 107, 202-218.

Patiño Douce, A. E. (2005). Vapor-absent melting of tonalite at 15–32 kbar. Journal of Petrology 46, 275-290.

Peck, W. H., Valley, J. W. & Graham, C. M. (2003). Slow oxygen diffusion rates in igneous zircons from metamorphic rocks. American Mineralogist 88, 1003-1014.

Putirka, K. D. (2008). Thermometers and barometers for volcanic systems. Reviews in Mineralogy and Geochemistry 69, 61-120.

Qian, Q. & Hermann, J. (2013). Partial melting of lower crust at 10-15 kbar Constraints on adakite and TTG formation. Contributions to Mineralogy and Petrology 165, 1195–1224.

Rapp, R. P. & Watson, E. B. (1995). Dehydration melting of metabasalt at 8–32 kbar: implications for continental growth and crust-mantle recycling. Journal of Petrology 36, 891-931.

Rapp, R. P., Shimizu, N. & Norman, M. D. (2003). Growth of early continental crust by partial melting of eclogite. Nature 425, 605-609.

Rogers, N., Macdonald, R., Fitton, J. G., George, R., Smith, M. & Barreiro, B. (2000). Two mantle plumes beneath the East African rift system: Sr, Nd and Pb isotope evidence from Kenya Rift basalts. Earth and Planetary Science Letters 176, 387-400.

Rosenberg, C. & Handy, M. (2005). Experimental deformation of partially melted granite revisited: implications for the continental crust. Journal of Metamorphic Geology 23, 19-28.

Royden, L. H., Burchfiel, B. C., King, R. W., Wang, E., Chen, Z., Shen, F. & Liu, Y. (1997). Surface deformation and lower crustal flow in eastern Tibet. Science 276, 788-790.
Rudnick, R. L. & Fountain, D. M. (1995). Nature and composition of the continental crust: a lower crustal perspective. Reviews of geophysics 33, 267-309.
Scaillet, B., Pichavant, M. & Roux, J. (1995). Experimental Crystallization of Leucogranite Magmas. Journal of Petrology 36, 663-705.
Searle, M., Cottle, J., Streule, M. & Waters, D. (2010). Crustal melt granites and migmatites along the Himalaya: melt source, segregation, transport and granite emplacement mechanisms. Geological Society of America Special Papers 472, 219-233.
Shapiro, N. M., Ritzwoller, M. H., Molnar, P. & Levin, V. (2004). Thinning and flow of Tibetan crust constrained by seismic anisotropy. Science 305, 233-236.
Shellnutt, J. G., Lee, T.-Y., Brookfield, M. E. & Chung, S.-L. (2014). Correlation between magmatism of the Ladakh Batholith and plate convergence rates during the India–Eurasia collision. Gondwana Research 26, 1051-1059.
Stegman, D., Freeman, J., Schellart, W., Moresi, L. & May, D. (2006). Influence of trench width on subduction hinge retreat rates in 3-D models of slab rollback. Geochemistry, Geophysics, Geosystems 7, Q03012, doi:10.1029/2005GC001056.
Stevens, G., Clemens, J. D. & Droop, G. T. (1997). Melt production during granulite-facies anatexis: experimental data from “primitive” metasedimentary protoliths. Contributions to Mineralogy and Petrology 128, 352-370.
Sylvester, P. J. (1998). Post-collisional strongly peraluminous granites. Lithos 45, 29-44.
Tatsumi, Y. & Kimura, N. (1991). Secular variation of basalt chemistry in the Kenya Rift: evidence for the pulsing of asthenospheric upwelling. Earth and Planetary Science Letters 104, 99-113.
Valley, J. W. (2003). Oxygen isotopes in zircon. Reviews in Mineralogy and Geochemistry 53, 343-385.
Valley, J. W., Kinny, P. D., Schulze, D. J. & Spicuzza, M. J. (1998). Zircon megacrysts from kimberlite: oxygen isotope variability among mantle melts. Contributions to Mineralogy and Petrology 133, 1-11.
Valley, J., Lackey, J., Cavosie, A., Clechenko, C., Spicuzza, M., Basei, M., Bindeman, I., Ferreira, V., Sial, A. & King, E. (2005). 4.4 billion years of crustal maturation: oxygen isotope ratios of magmatic zircon. Contributions to Mineralogy and Petrology 150, 561-580.
Vervoort, J. D. & Blichert-Toft, J. (1999). Evolution of the depleted mantle: Hf isotope evidence from juvenile rocks through time. Geochimica et Cosmochimica Acta 63, 533-556.
von Blanckenburg, F. & Davies, J. H. (1995). Slab breakoff: A model for syncollisional magmatism and tectonics in the Alps. Tectonics 14, 120-131.
Wang, Q., Chung, S.-L., Li, X.-H., Wyman, D., Li, Z.-X., Sun, W.-D., Qiu, H.-N., Liu, Y.-S. & Zhu, Y.-T. (2012). Crustal melting and flow beneath northern Tibet: evidence from Mid-Miocene to Quaternary strongly peraluminous rhyolites in the southern Kunlun range. Journal of Petrology 53, 2523-2566.
Wang, Q., Hawkesworth, C. J., Wyman, D., Chung, S.-L., Wu, F.-Y., Li, X.-H., Li, Z.-X., Gou, G.-N., Zhang, X.-Z., Tang, G.-J., Dan, W., Ma, L. & Dong, Y.-H. (2016). Pliocene-Quaternary crustal melting in central and northern Tibet and insights into crustal flow. Nature Communications 7, doi: 10.1038/ncomms11888.
Wang, R., Richards, J. P., Hou, Z.-q., An, F. & Creaser, R. A. (2015). Zircon U–Pb age and Sr–Nd–Hf–O isotope geochemistry of the Paleocene–Eocene igneous rocks in western Gangdese: evidence for the timing of Neo-Tethyan slab breakoff. Lithos 224, 179-194.
Wen, D.-R., Liu, D., Chung, S.-L., Chu, M.-F., Ji, J., Zhang, Q., Song, B., Lee, T.-Y., Yeh, M.-W. & Lo, C.-H. (2008). Zircon SHRIMP U–Pb ages of the Gangdese Batholith and implications for Neotethyan subduction in southern Tibet. Chemical Geology 252, 191-201.
White, A. J. & Chappell, B. W. (1977). Ultrametamorphism and granitoid genesis. Tectonophysics 43, 7-22.
White, L. T. & Lister, G. S. (2012). The collision of India with Asia. Journal of Geodynamics 56, 7-17.
Wu, F., Liu, X., Ji, W., Wang, J. & Yang, L. (2017). Highly fractionated granites: Recognition and research. Science China Earth Sciences 60, 1201-1219. doi: 10.1007/s11430-016-5139-1.

Wu, F.-y., Jahn, B.-m., Wilde, S. A., Lo, C.-H., Yui, T.-F., Lin, Q., Ge, W.-c. & Sun, D.-y. (2003). Highly fractionated I-type granites in NE China (I): geochronology and petrogenesis. Lithos 66, 241-273.

Wu, F.-Y., Ji, W.-Q., Wang, J.-G., Liu, C.-Z., Chung, S.-L. & Clift, P. D. (2014). Zircon U–Pb and Hf isotopic constraints on the onset time of India-Asia collision. American Journal of Science 314, 548-579.

Xiong, X., Adam, J. & Green, T. (2005). Rutile stability and rutile/melt HFSE partitioning during partial melting of hydrous basalt: implications for TTG genesis. Chemical Geology 218, 339-359.

Xu, Y.-G., Luo, Z.-Y., Huang, X.-L., He, B., Xiao, L., Xie, L.-W. & Shi, Y.-R. (2008). Zircon U–Pb and Hf isotope constraints on crustal melting associated with the Emeishan mantle plume. Geochimica et Cosmochimica Acta 72, 3084-3104.

Yi, Z., Huang, B., Chen, J., Chen, L. & Wang, H. (2011). Paleomagnetism of early Paleogene marine sediments in southern Tibet, China: Implications to onset of the India–Asia collision and size of Greater India. Earth and Planetary Science Letters 309, 153-165.

Yin, A. & Harrison, T. M. (2000). Geologic evolution of the Himalayan-Tibetan orogen. Annual Review of Earth and Planetary Sciences 28, 211-280.

Zeng, L., Gao, L.-E., Xie, K. & Liu-Zeng, J. (2011). Mid-Eocene high Sr/Y granites in the Northern Himalayan Gneiss Domes: melting thickened lower continental crust. Earth and Planetary Science Letters 303, 251-266.

Zhang, H., Harris, N., Parrish, R., Kelley, S., Zhang, L., Rogers, N., Argles, T. & King, J. (2004). Causes and consequences of protracted melting of the mid-crust exposed in the North Himalayan antiform. Earth and Planetary Science Letters 228, 195-212.

Zhang, Z., Dong, X., Xiang, H., Ding, H., He, Z. & Liou, J. (2015). Reworking of the Gangdese magmatic arc, southeastern Tibet: post‐collisional metamorphism and anatexis. Journal of Metamorphic Geology 33, 1-21.

Zhang, Z., Dong, X., Xiang, H., Liou, J. & Santosh, M. (2013). Building of the deep Gangdese arc, south Tibet: Paleocene plutonism and granulite-facies metamorphism. Journal of Petrology 54, 2547-2580.

Zhu, D. C., Wang, Q., Cawood, P. A., Zhao, Z. D. & Mo, X. X. (2017). Raising the Gangdese Mountains in southern Tibet. Journal of Geophysical Research: Solid Earth 122, doi:10.1002/2016JB013508.

Zhu, D. C., Zhao, Z. D., Niu, Y., Mo, X. X., Chung, S. L., Hou, Z. Q., Wang, L. Q. & Wu, F. Y. (2011). The Lhasa Terrane: Record of a microcontinent and its histories of drift and growth. Earth and Planetary Science Letters 301, 241-255.

Zhu, D.-C., Wang, Q., Zhao, Z.-D., Chung, S.-L., Cawood, P. A., Niu, Y., Liu, S.-A., Wu, F.-Y. & Mo, X.-X. (2015). Magmatic record of India-Asia collision. Scientific Reports 5, 14298. doi:10.1038/srep14289

Zhu, D.-C., Zhao, Z.-D., Niu, Y., Dilek, Y., Hou, Z.-Q. & Mo, X.-X. (2013). The origin and pre-Cenozoic evolution of the Tibetan Plateau. Gondwana Research 23, 1429-1454.

FIGURE CAPTIONS

Fig. 1. (a) Geological map of the Lhasa Block (modified from Chung *et al.* (2009)). Abbreviations: SNMZ = Shiquan River–Nam Tso Mélange Zone; LMF = Luobadui–Milashan Fault; BNS = Bangong–Nujiang suture; IYTS = Indus–Yarlung Tsangpo Suture; MCT = Main Central Thrust; MBT= Main Boundary Thrust; STDS = South Tibet Detachment System. (b) Detailed occurrences of Paleocene magmatic rocks in the Xigaze–Nyingchi section of the Gangdese batholith. Yellow ovals mark the locations of zircon U–Pb isotopic ages of the Paleocene magmatic rocks (including published data and from this study) and further details are listed in Supplementary Data File 1. (c) A geological map of the Sangri area showing the sampling locations in this study and the location of published zircon U–Pb isotopic ages of the Gangdese magmatic rocks. Details are listed in Supplementary Data File 1.

Fig. 2. Field geological characteristics and petrography of the Zhengga garnet-bearing two-mica granites and biotite granites: (a) field outcrop of granitic intrusive rocks; (b) massive garnet-bearing granites; (c) main mineral assemblage of the garnet-bearing granite; (d) garnets associated with plagioclase and muscovite; (e) coexisting garnet, muscovite, biotite and quartz; (f) intergrown muscovite, biotite and plagioclase; (g) polycrystalline garnet; (h) main mineral assemblage of the biotite granite; and (i) two types of biotite in the biotite granite. Abbreviations: Pl - plagioclase; Grt - garnet; Bi - biotite; Ms - muscovite; Qtz - quartz and Cal - calcite.

Fig. 3. (a) Back–scattered–electron (BSE) image; (b) Al; (c) Na and (d) Ca chemical mapping of plagioclase grains from a Zhengga biotite granites.

Fig. 4. Variations and core-mantle-rim structure of the plagioclase grains in a Zhengga biotite granite. (a-c) and garnet-bearing two-mica granite (d-f). Circles indicate the locations of analyzed sites. Abbreviation: Ab-albite; An-anorthite.

Fig. 5. (a-c) Mn; (d-f) Fe and (g-i) Ca chemical mapping of garnet grains from the Zhengga garnet-bearing two-mica granites.

Fig. 6. LA-ICP-MS and SIMS zircon U–Pb concordia diagrams with CL images for biotite granite (a) 11SR05-1, (b) 11SR03 and (c) 11SR04 , and garnet-bearing granites (d) 11SR01-2, (e) 09TB66 and (f) 11SR05-2.

Fig. 7. (a) SiO_2 vs. Na_2O+K_2O classification diagram (after Middlemost (1994)); (b) SiO_2 vs. K_2O (after Peccerillo & Taylor (1976)); (c) A/CNK vs. A/NK classification diagram (after Shand (1951)); (d) Normative minerals (An-Ab-Or) of the Himalayan leucogranite (modified from Wu *et al.* (2014)). All plotted data were recalculated to 100 wt % on a volatile-free basis. Data resource: Jurassic Central Lhasa (CL) leucogranites are from Liu *et al.* (2006); Paleocene Southern Lhasa (SL) igneous rocks are from Wen (2007), Lee *et al.* (2012), Zhang *et al.* (2013) and Jiang *et al.*

(2014); Eocene Tethyan Himalaya (TH) granites are from Zeng *et al.* (2011) and Liu *et al.* (2014); Miocene High Himalaya (HH) leucogranites are from Harris *et al.* (2002), King *et al.* (2003, 2004), Zhang *et al.* (2004) and Guo & Wilson (2012).

Fig. 8. Primitive mantle-normalised trace element and chondrite-normalised REE patterns of the Zhengga garnet-bearing granites and biotite granites. Data source: Jurassic Central Lhasa (CL) leucogranites - Liu *et al.* (2006); Paleocene Southern Lhasa (SL) I-type granites - Wen (2007), Lee *et al.* (2012), Zhang *et al.* (2013) and Jiang *et al.* (2014); Paleocene Southern Lhasa (SL) S-type granites - Zhang *et al.* (2013); Eocene Tethyan Himalaya (TH) granites - Zeng et al. (2011); Miocene High Himalaya (HH) leucogranites - Guo & Wilson (2012). Chondrite and primitive mantle normalization values are from Sun & McDonough (1989).

Fig. 9. (a) $\varepsilon_{Nd}(t)$ vs. $(^{87}Sr/^{86}Sr)_i$ diagram for the Zhengga garnet-bearing granites and biotite granites. Data sources are as in Fig. 7. Additional data sources: IYTS ophiolites - Mahoney *et al.* (1998) and Zhang *et al.* (2005); Miocene HH leucogranites - Guo & Wilson (2012); Eocene TH granites - Zeng *et al.* (2011) and Liu et al. (2014); Eocene to Miocene SL adakites - Chung *et al.* (2003), Hou *et al.* (2004), Guo *et al.* (2007) and Jiang *et al.* (2014); Cretaceous SL magmatic rocks - Wen *et al.* (2008), Ma *et al.* (2013a, b, c, 2015). The mixing endmembers are: SL Juvenile lower crust (09TB79: $\varepsilon_{Nd}(T)$=+3.8, $(^{87}Sr/^{86}Sr)_i$ = 0.7045, Nd=6.16 ppm and Sr=852.4 ppm) from Ma *et al.* (2013); global subducting sediment (GLOSS: $\varepsilon_{Nd}(T)$ = -8.6, $(^{87}Sr/^{86}Sr)_i$ = 0.7170, Nd = 27 ppm, Sr = 327 ppm) from Plank & Langmuir (1998); Devonian granite (11SR02-3) representing the ancient Gangdese crust ($\varepsilon_{Nd}(T)$ = -11.0, $(^{87}Sr/^{86}Sr)_i$ = 0.7274, Nd = 26 ppm, Sr = 131 ppm; Table 3); HH crystalline basement (NL07: $\varepsilon_{Nd}(T)$ = -15.6, $(^{87}Sr/^{86}Sr)_i$ = 0.7357, Nd = 11 ppm, Sr = 89 ppm) from Guo & Wilson (2012); (b) zircon $\delta^{18}O$ vs. $\varepsilon_{Hf}(t)$ diagram. Average $\delta^{18}O$ value of mantle magmas (5.3 ± 0.3‰, 1SD) are from Valley *et al.* (1998). Data sources: Cretaceous Zhengga gabbros - Ma *et al.* (2013a); Paleocene Yajie gabbros - Wang *et al.* (2015). (c) zircon $\varepsilon_{Hf}(t)$ vs. $\varepsilon_{Nd}(t)$ diagrams. Data sources: Gangdese batholith - Ji *et al.* (2009) and Zhu *et al.* (2011); I-type granites - Ji *et al.* (2014); Paleocene I-type granites - Zhang *et al.* (2013), Wang *et al.* (2015) and Ji *et al.* (2015); Paleocene S-type granites - Zhang *et al.* (2013). (d) zircon $\delta^{18}O$ vs. Nb/U diagram.

Fig.10. SiO_2 vs. (a) Al_2O_3; (b) $Fe_2O_3^{T\ (total)}$; (c) P_2O_5; (d) Eu/Eu*; (e) Nb/La and (f) Sr/Y diagrams for the Paleocene Zhengga granites. The trends of I-type and S-type granites are from Chappell & White (1992).

Fig.11. Equilibrium (batch) melting modelling results for Zhengga biotite granites from southern Lhasa. Melting of 95% juvenile mafic lower crust (average of the Zhengga gabbros; Ma *et al.*, 2013b) + 5% ancient crust (average of the Devonian granites given in Supplementary Data File 7). Patterns with symbols are modelling results (5% melting increments). The source composition comprises 40% plagioclase, 45% amphibole and 15% clinopyroxene. Partition coefficients of plagioclase

amphibole and clinopyroxene are from McKenzie & O'Nions (1991). REE data of the initial material and partition coefficients are given in Supplementary File 7.

Fig.12. (a) Ba/Sr vs. Sr and (b) Ba vs. Sr. The grey dashed lines are composition trends showing that fractionation of plagioclase plays an important role in the earliest stage of differentiation; whereas in the later stage, separation of K-feldspar and minor plagioclase, appears to have controlled the variation of these elements. Partition coefficients and calculated composition of K, Rb, S and Ba are listed in Supplementary Data File 7.

Fig.13. (a) La/Yb versus Sr/Y diagram (after Wang *et al.* (2016)). This diagram indicates the effects of residual garnet (Grt) and plagioclase (Pl) during partial melting (for discussion see the text). Field 1: adakitic melts derived from eclogitic rocks in the stability field of garnet with little or no plagioclase; Field 2: crustal melts in the stability field of plagioclase and garnet; Field 3: crustal melts in the stability field of plagioclase with little or no garnet. (b) Pressure–temperature conditions for partial melting of crustal rocks. Curves or lines for melting or mineral stability: (1) H_2O-saturated or wet solidus curve of crustal rocks (Xiong *et al.*, 2005; Patiño Douce,2005; Qian & Hermann, 2013); (2) dehydration solidi curve for crustal rocks (17,47); (3) dry solidus curve (Qian & Hermann, 2013); (4) garnet-in/out curve during dehydration melting of metabasalts (Rapp & Watson, 1995; Patiño Douce & Harris, 1998; Rapp *et al.*, 2003; Patiño Douce, 2005; Xiong *et al.*, 2005; Nair & Chacko, 2008); (5) garnet proportion contours (5 and 20 wt %) in the residue of metabasalt melting (Nair & Chacko, 2008); (6) rutile-in/out curve (Xiong et al., 2005); (7) plagioclase-in (beneath curve)/out (above curve) curve during dehydration melting (Rapp et al., 2003; Qian & Hermann, 2013); (8) orthopyroxene-in (beneath curve)/out (above curve) curve during dehydration melting (Qian & Hermann, 2013); (9) the boundary line for garnet-bearing (above line) and cordierite-rich (beneath line) melts during dehydration melting of metasedimentary rocks (Green, 1977; Clemens & Wall, 1981; Wang *et al.*, 2012); (10) upper thermal stability of F-free mica in pelite, wacke, mica schist and tonalite (Hacker *et al.*, 2014; Douce & Harris, 1998; Patiño Douce, 2005).

Fig.14. A model for interaction between diachronous continental collision and subducted oceanic slab roll-back causing crustal anatexis, crustal thickening, metamorphism and possible crustal flow along the southern margin of the Tibetan Plateau during the Early Paleocene (ca. 63 Ma). The Paleocene biotite granite magmas were formed by anatexis in the middle-lower crust (~40-15 km) and subsequently some upwelled to middle-upper crust levels (~20-10 km), which resulted in widespread large-scale granitic chambers or magma reservoirs in lower to shallow crust levels (40-10 km). The Zhengga garnet-bearing two-mica granites represent highly evolved magmas that formed in shallow crustal chambers. Greater India boundary is after Hall (2002), Zhou & Murphy (2005) and Ali & Aitchison (2005).

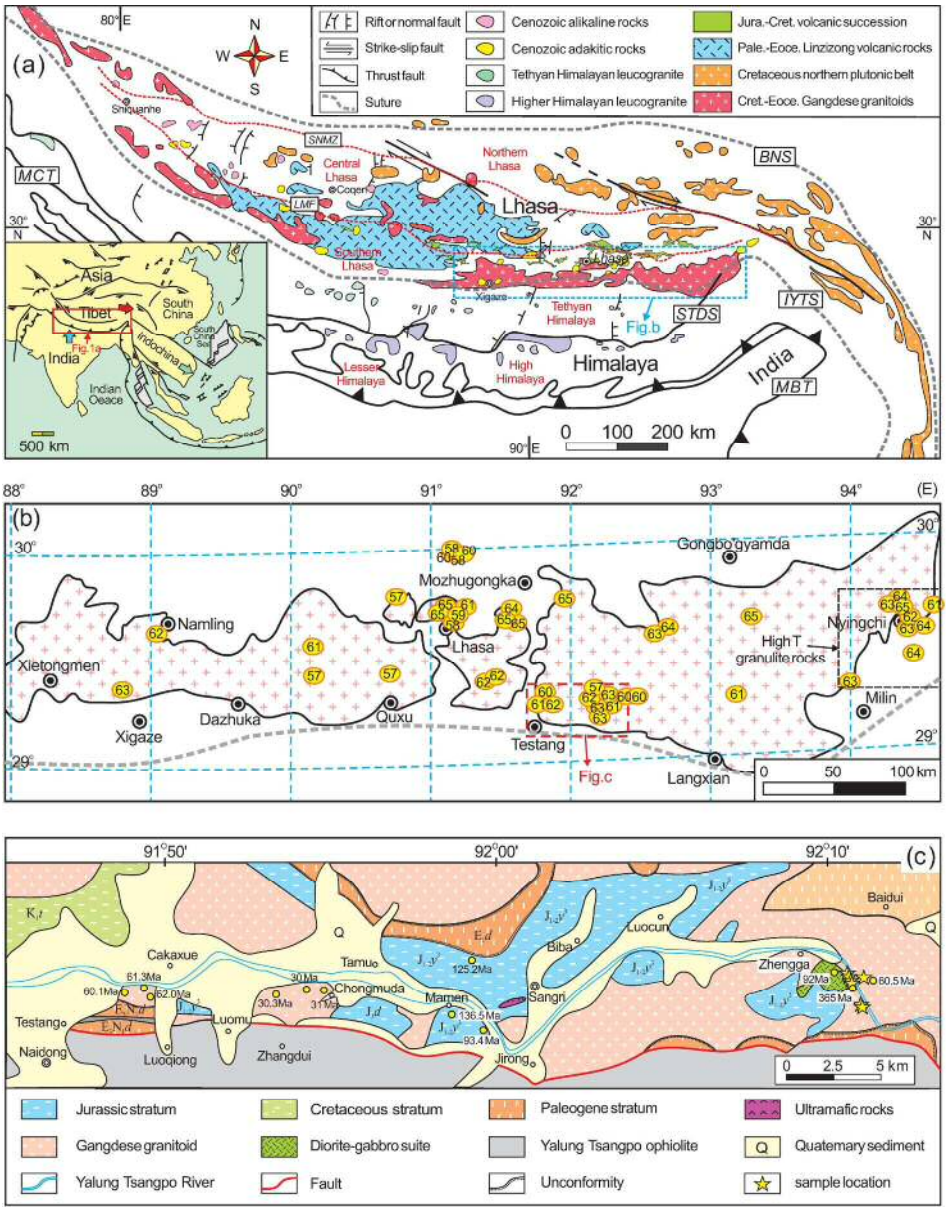

Figure 1

312x397mm (300 x 300 DPI)

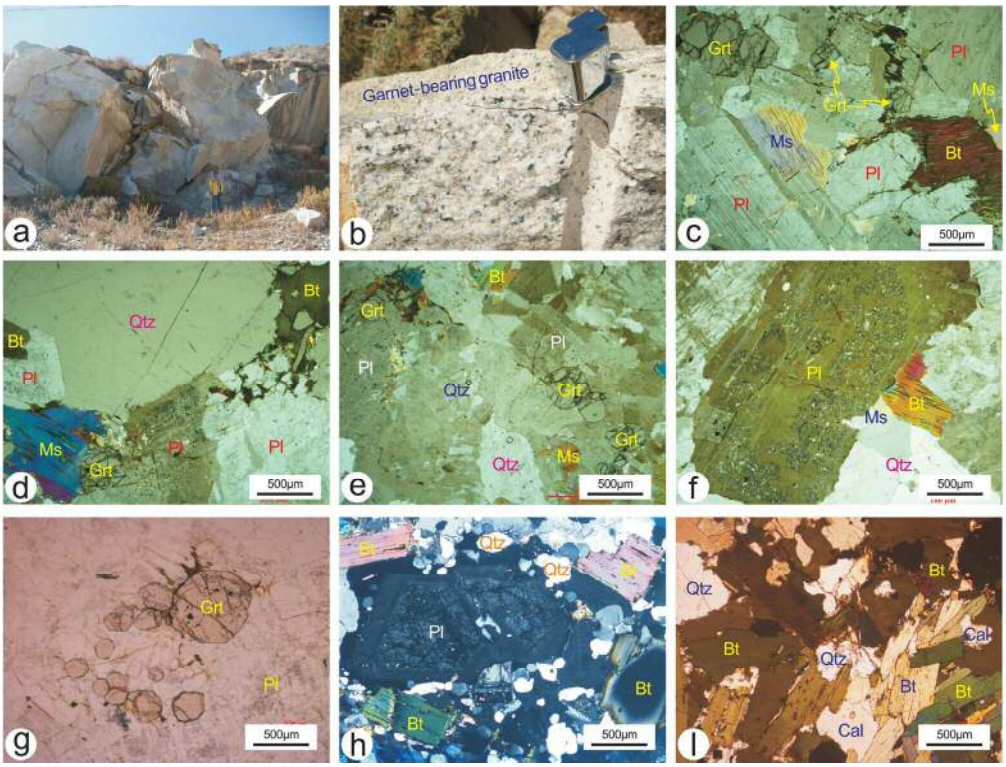

Figure 2

150x113mm (300 x 300 DPI)

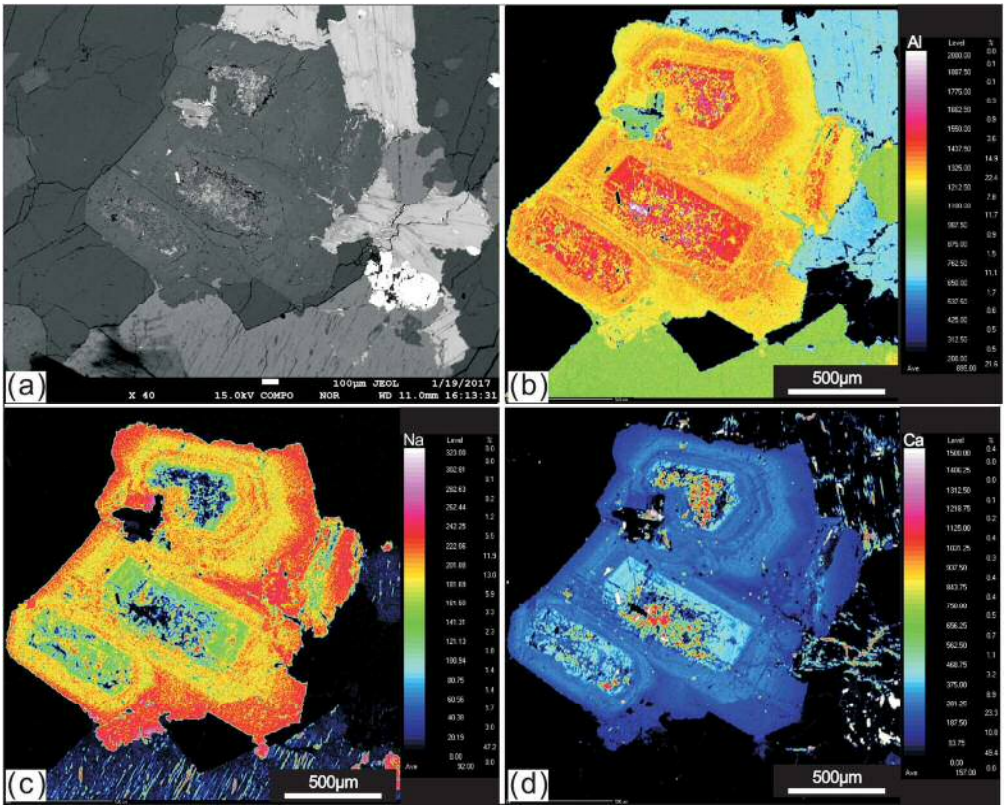

Figure 3

154x123mm (300 x 300 DPI)

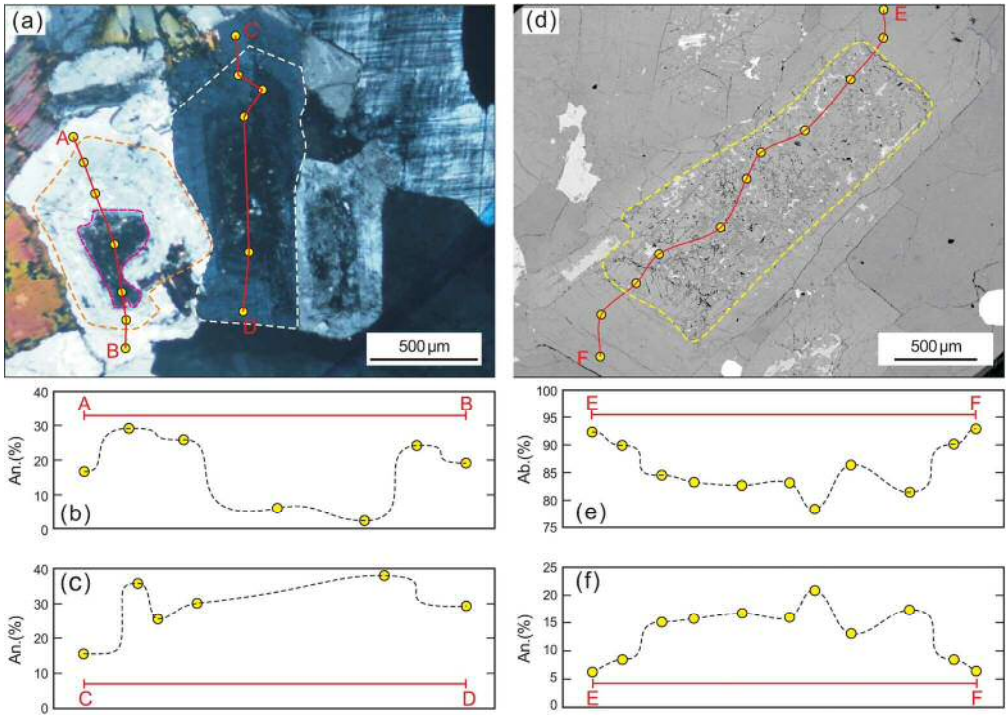

Figure 4

151x107mm (300 x 300 DPI)

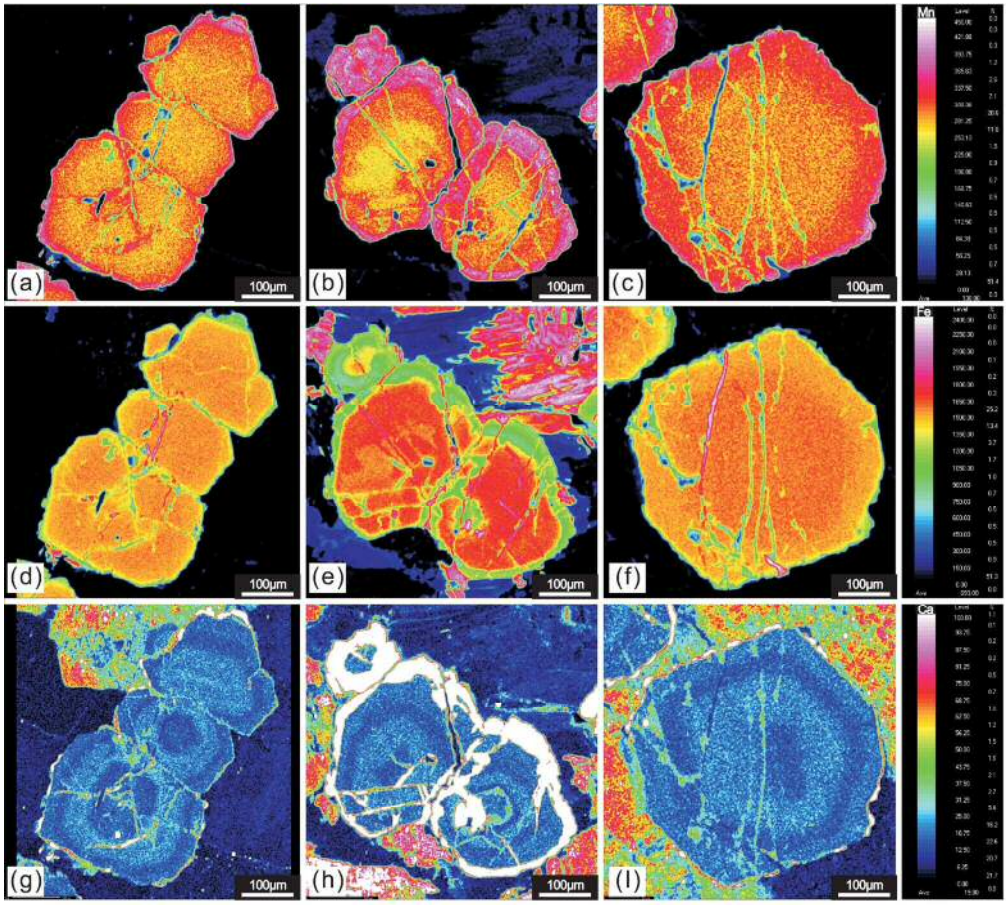

Figure 5

183x165mm (300 x 300 DPI)

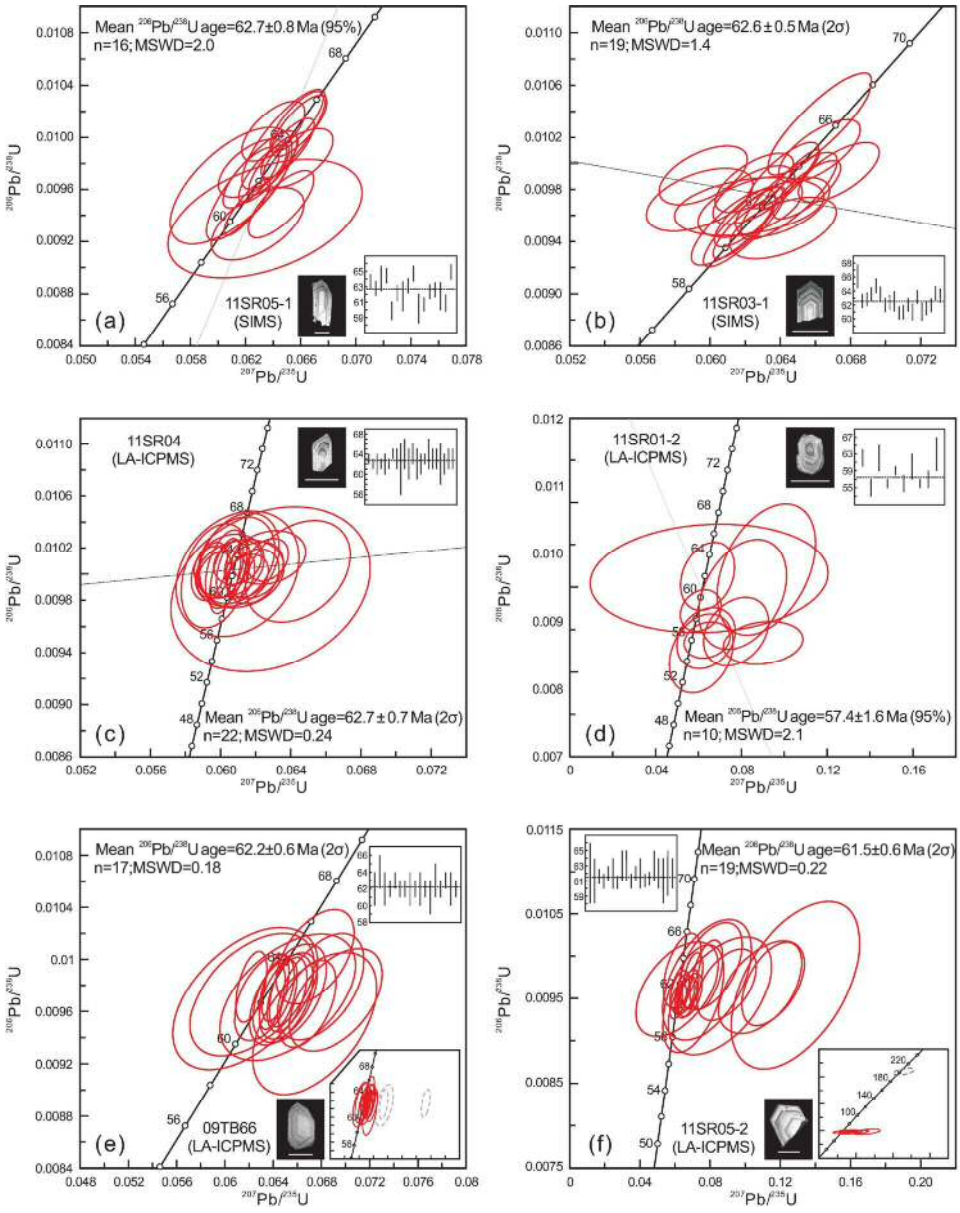

Figure 6

262x330mm (300 x 300 DPI)

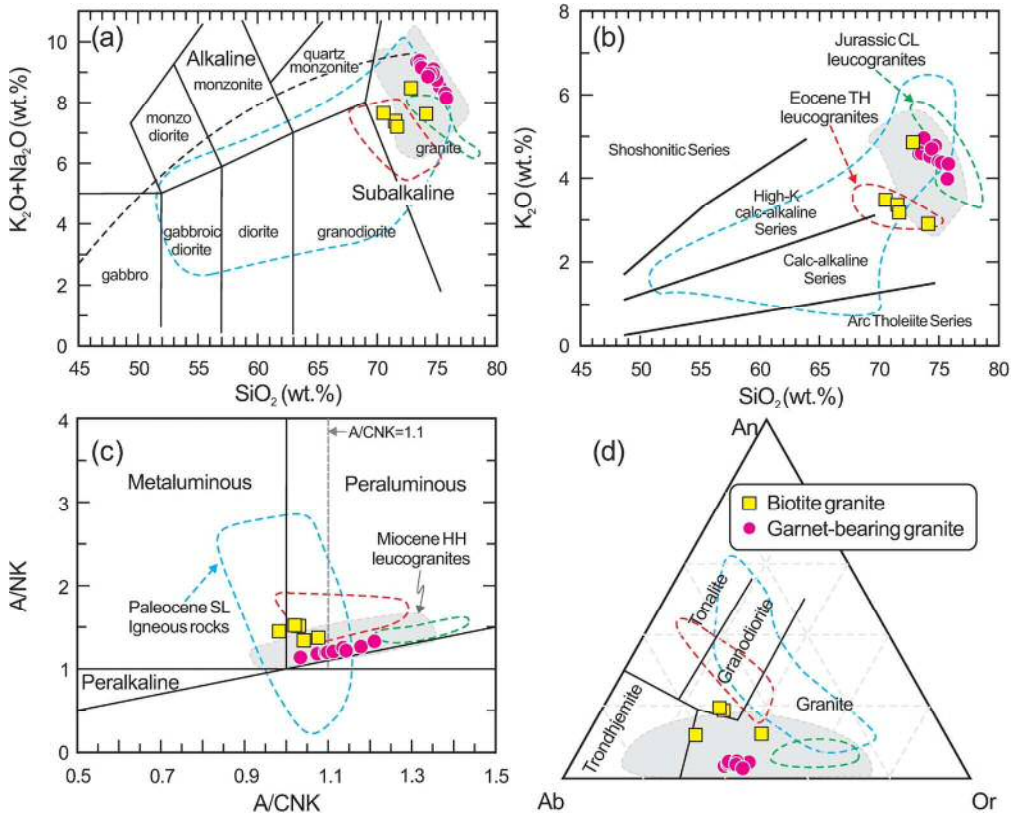

Figure 7

162x131mm (300 x 300 DPI)

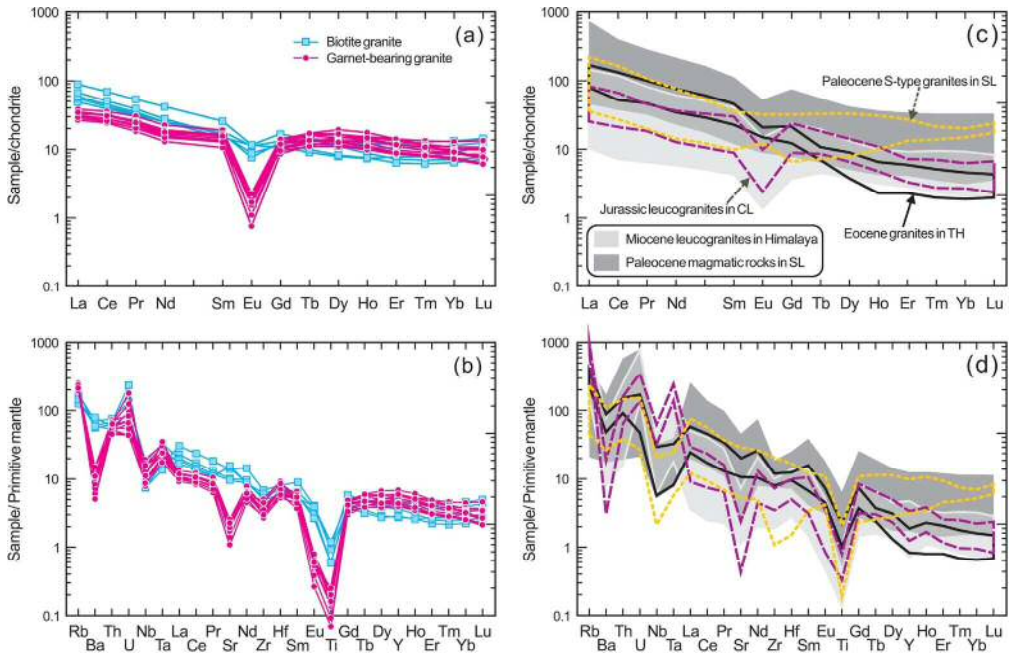

Figure 8

168x108mm (300 x 300 DPI)

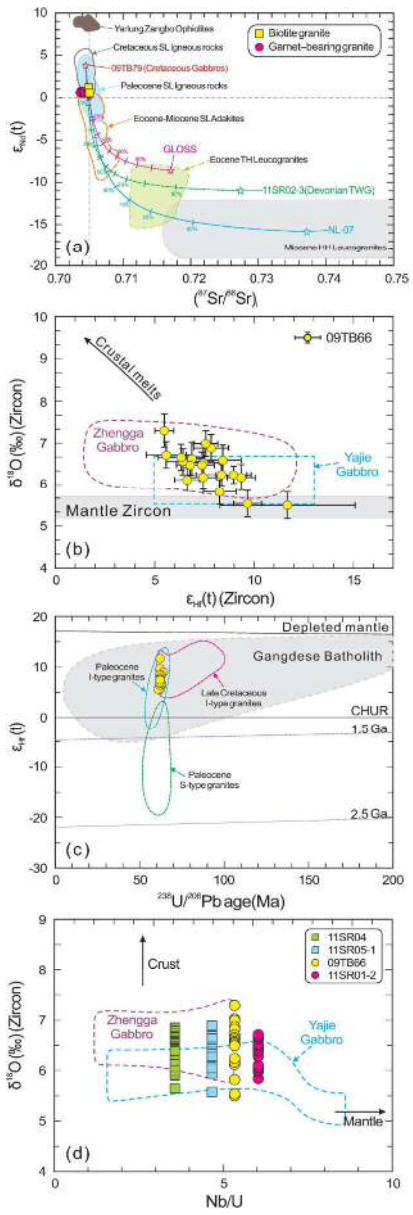

Figure 9

464x1385mm (300 x 300 DPI)

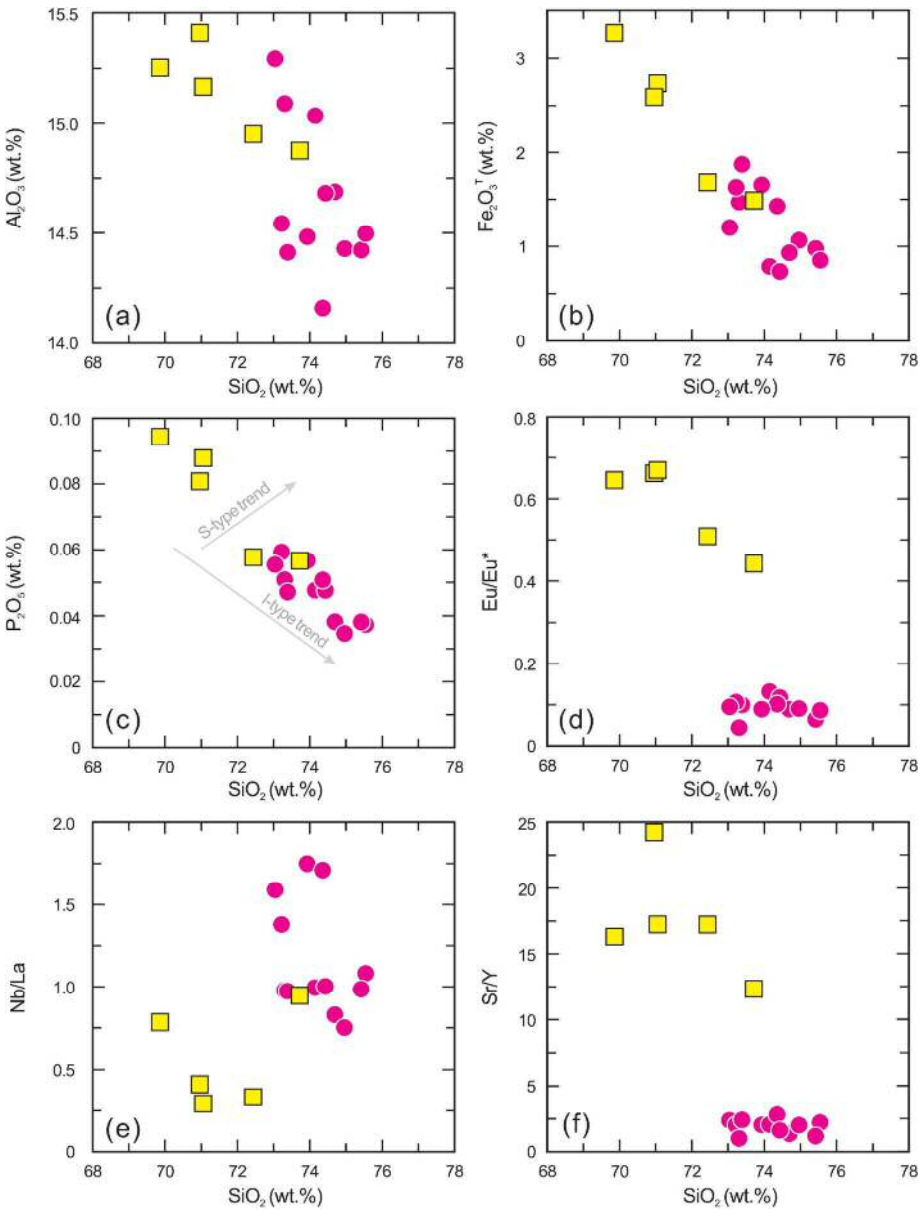

Figure 10

252x331mm (300 x 300 DPI)

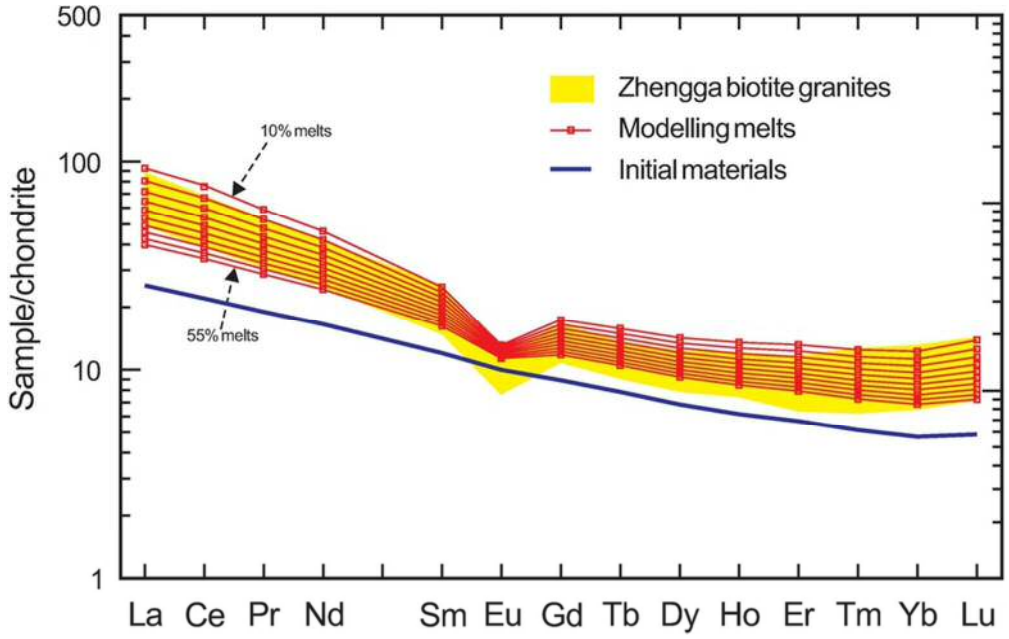

Figure 11

80x50mm (300 x 300 DPI)

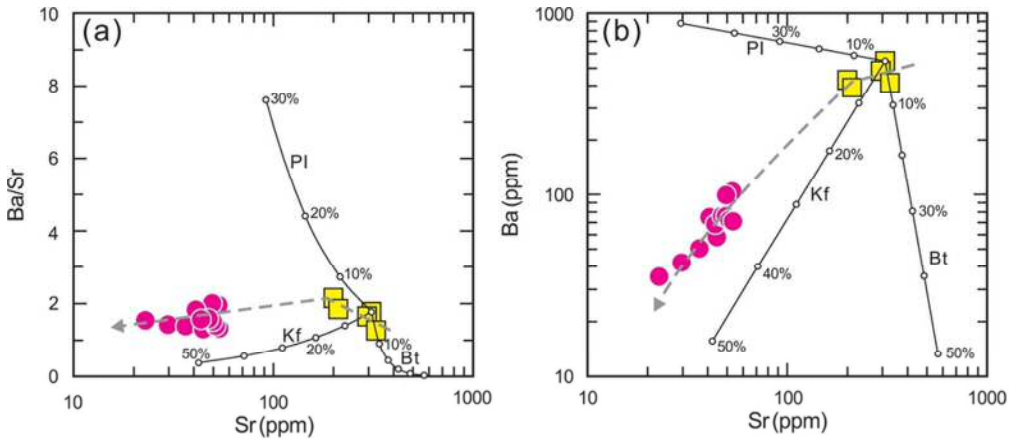

Figure 12

82x35mm (300 x 300 DPI)

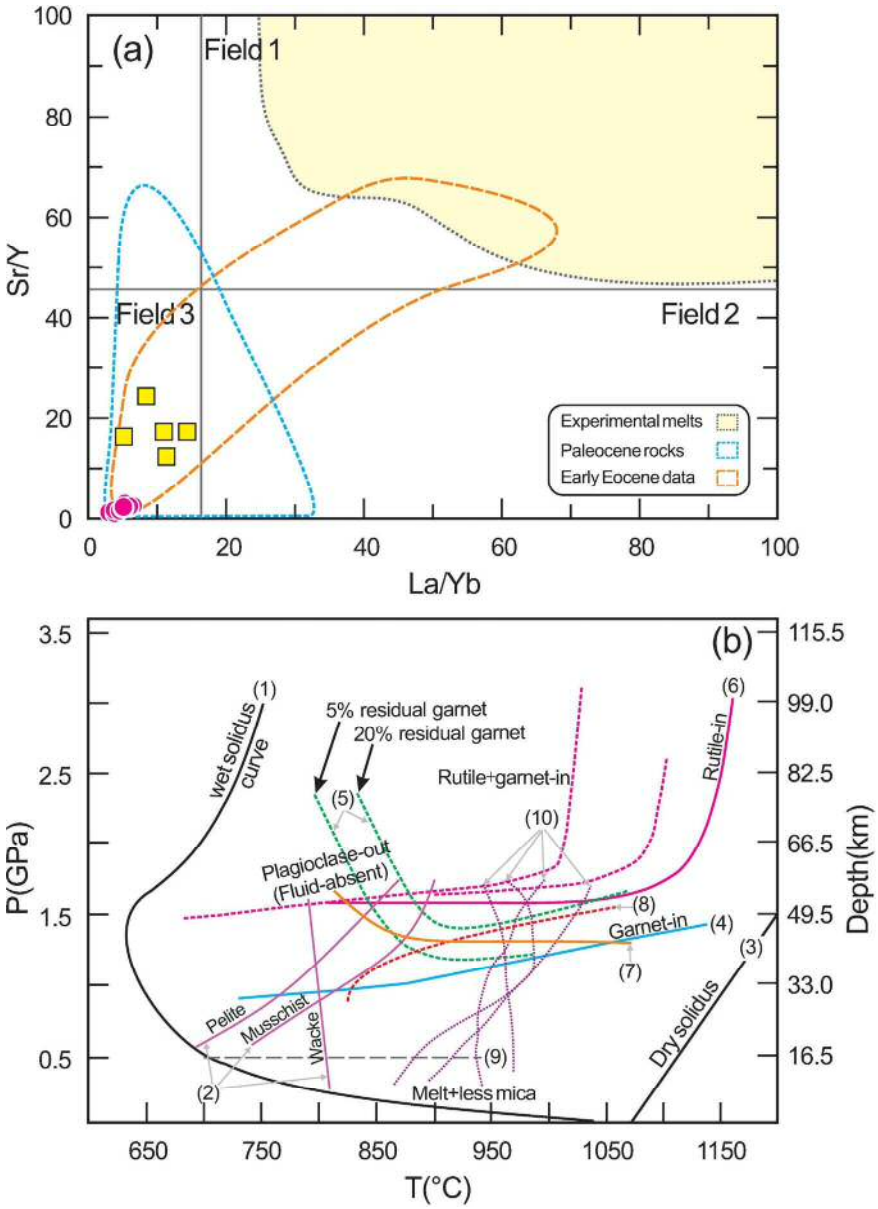

Figure 13

188x259mm (300 x 300 DPI)

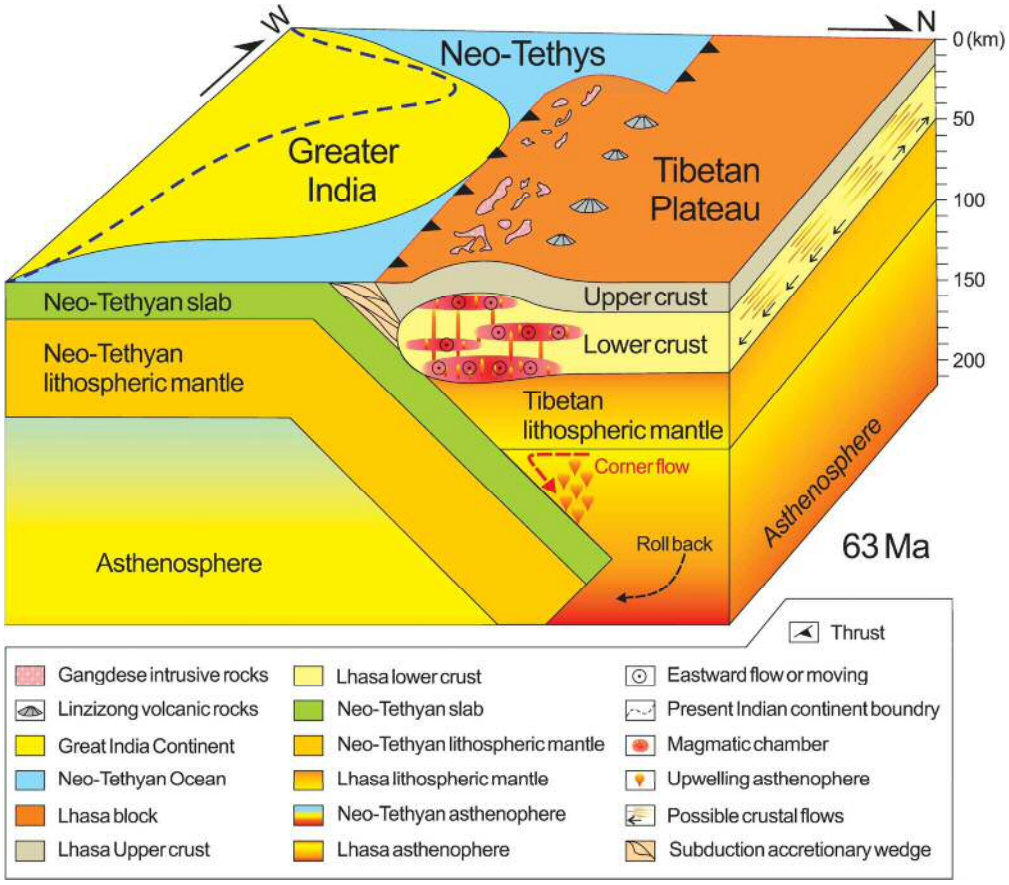

Figure 14

213x187mm (300 x 300 DPI)

Table 1 Samples and brief description

Sample	Rock type	Latitude	Longitude	Mineralogy
09TB66	GBG	92°10'31"	29°15'56"	Pl +Qtz+Kf+Gt+Bt+Ms+Chl
11SR01-1	GBG	92°10'30.1"	29°15'56.5"	Pl +Qtz+Kf+Gt+Bt+Ms
11SR01-2	GBG	92°10'30.1"	29°15'56.5"	Pl +Qtz+Kf+Gt+Bt+Ms
11SR01-3	GBG	92°10'30.1"	29°15'56.5"	Pl +Qtz+Kf+Gt+Bt+Ms
11SR05-2	GBG	92°10'57"	29°15'20"	Pl +Qtz+Kf+Gt+Bt+Ms
11SR05-3	GBG	92°10'57"	29°15'20"	Pl +Qtz+Kf+Gt+Bt+Ms
16ML06-1	GBG	92°10′32.7″	29°15′54.1″	Pl +Qtz+Kf+Gt+Bt+Ms+Mt
16ML06-2	GBG	92°10′32.7″	29°15′54.1″	Pl +Qtz+Kf+Gt+Bt+Ms
16ML07-1	GBG	92°10′31.5″	29°15′54.8″	Pl +Qtz+Kf+Gt+Bt+Ms
16ML08-1	GBG	92°10′30.2″	29°15′56.1″	Pl +Qtz+Kf+Gt+Bt+Ms
16ML08-2	GBG	92°10′30.2″	29°15′56.1″	Pl +Qtz+Kf+Gt+Bt+Ms
16ML09-1	GBG	92°10′30.8″	29°15′55.9″	Pl +Qtz+Kf+Gt+Bt+Ms
11SR03	BG	92°10'35"	29°15'52"	Pl+Kf+Qtz+Bt+Ttn
11SR04	BG	92°10'54"	29°15'25"	Pl+Kf+Qtz+Bt+Ms (min)
11SR05-1	BG	92°10'57"	29°15'20"	Pl+Kf+Qtz+Bt+Ms (min)
11SR06	BG	92°10'33"	29°16'04"	Pl+Kf+Qtz+Bt
16ML02-1	BG	92°10′34.2″	29°15′52.1″	Pl+Kf+Qtz+Bt+Ms (min)
11SR02-1	TMG	92°10'33"	29°15'54"	Pl+Kf+Qtz+Bt+Ms+Gt (min)
11SR02-3	TMG	92°10'33"	29°15'54"	Pl+Kf+Qtz+Bt+Ms

GBG = garnet-bearing two-mica granite; BG = biotite granite; TMG = (Devonian) two-mica granite; Pl = plagioclase; Kf = potassium feldspar; Qtz = quartz; Gt = garnet; Bt = biotite; Ms = muscovite; Chl = chlorite; Ap = apatite; Ttn = titanite; Mt = Ti-bearing magnetite.

Table 2 Major (wt %) and trace element (ppm) data for the Zhengga leucogranites and associated rocks

Sample No.	09TB66	11SR01-1	11SR01-2	11SR01-3	11SR05-2	11SR05-3	16ML06-1	16ML06-2	16ML07-1
Rock type	GBG	GBG	GBG	GBG	GBG	GBG	GBG	GBG	GBG
SiO_2	75.01	75.64	74.92	75.11	73.99	73.63	72.70	73.05	73.62
TiO_2	0.05	0.02	0.03	0.03	0.03	0.06	0.04	0.01	0.06
Al_2O_3	14.39	14.46	14.73	14.46	14.59	14.93	15.22	15.04	14.42
$Fe_2O_3^T$	0.85	0.98	0.94	1.07	0.73	0.78	1.19	1.47	1.65
MnO	0.13	0.19	0.18	0.13	0.15	0.12	0.18	0.23	0.21
MgO	0.19	0.18	0.18	0.21	0.21	0.21	0.23	0.21	0.22
CaO	0.58	0.48	0.54	0.64	0.65	0.67	0.65	0.45	0.57
Na_2O	3.76	4.31	4.35	4.16	4.28	4.20	4.72	4.33	4.30
K_2O	4.29	3.98	4.40	4.36	4.72	4.65	4.54	4.82	4.48
P_2O_5	0.04	0.04	0.04	0.03	0.05	0.05	0.06	0.05	0.06
L.O.I	0.58	0.54	0.49	0.58	0.38	0.48	0.43	0.34	0.39
Total	99.87	99.87	99.87	99.87	99.87	99.87	99.87	99.87	99.87
A/CNK	1.21	1.18	1.14	1.14	1.09	1.13	1.10	1.14	1.11
Sc	1.18	3.48	4.18	5.41	6.20	5.33	2.41	2.59	2.82
V	13.6	11.8	17.1	16.3	12.7	18.9	5.02	3.58	5.81
Cr	1.64	66.5	108	153	130	150	7.56	12.5	29.2
Ni	1.77	4.97	6.01	7.26	6.29	6.27	1.02	1.97	2.33
Rb	127	127	147	123	142	144	156	145	158
Sr	51.5	29.6	36.4	43.5	49.5	53.1	44.5	22.9	41.0
Y	23.3	25.1	26.9	21.6	30.8	25.8	18.7	22.9	20.3
Zr	36.7	55.8	35.8	39.7	42.1	43.4	37.0	32.1	39.1
Nb	8.32	6.61	6.86	5.49	7.08	8.94	11.6	6.09	13.7

Cs	4.08	6.16	6.49	4.55	4.00	3.90	7.36	6.02	7.49
Ba	72.0	42.0	50.4	68.0	99.2	104	58.2	35.2	74.9
La	7.70	6.71	8.27	7.31	7.07	8.99	7.33	6.23	7.83
Ce	19.0	15.4	18.9	16.7	16.7	21.5	17.0	14.6	19.1
Pr	2.36	1.91	2.37	2.05	2.17	2.85	2.05	1.72	2.44
Nd	8.30	7.02	8.56	7.71	8.06	10.4	7.32	6.04	8.86
Sm	2.43	1.94	2.51	2.22	2.43	2.89	2.06	1.62	2.48
Eu	0.09	0.06	0.09	0.09	0.12	0.13	0.09	0.04	0.09
Gd	2.72	2.19	2.80	2.57	2.80	2.94	2.09	1.77	2.47
Tb	0.58	0.49	0.59	0.52	0.64	0.59	0.45	0.42	0.51
Dy	3.74	3.71	4.14	3.43	4.84	4.16	2.96	3.38	3.32
Ho	0.73	0.86	0.85	0.70	0.99	0.80	0.58	0.76	0.63
Er	1.81	2.32	2.17	1.61	2.32	1.96	1.41	1.90	1.50
Tm	0.25	0.34	0.29	0.23	0.30	0.27	0.20	0.28	0.21
Yb	1.49	2.18	1.82	1.44	1.82	1.69	1.22	1.62	1.29
Lu	0.19	0.34	0.27	0.22	0.26	0.25	0.15	0.19	0.16
Hf	1.61	2.80	1.68	2.01	2.09	2.06	2.00	1.84	2.14
Ta	1.10	0.82	0.88	0.88	0.83	0.95	1.21	0.71	1.27
Pb	22.2	17.0	20.8	28.9	24.4	25.2	18.0	18.4	17.8
Th	4.81	4.26	4.85	4.72	4.75	6.07	4.47	4.11	5.66
U	1.56	1.35	1.14	1.97	1.52	1.73	0.91	0.91	1.39
Eu/Eu*	0.10	0.09	0.10	0.12	0.14	0.14	0.14	0.08	0.11
T_{Zr}(℃)	629	661	619	627	626	633	614	608	622

Table 2 (continued)

Sample No.	16ML08-1	16ML08-2	16ML09-1	11SR03	11SR04	11SR05-1	11SR06	16ML02-1
Rock type	GBG	GBG	GBG	BG	BG	BG	BG	BG
SiO_2	74.08	72.85	73.14	70.57	71.87	73.16	70.36	69.67
TiO_2	0.05	0.05	0.05	0.26	0.15	0.14	0.23	0.26
Al_2O_3	14.11	14.47	14.36	15.06	14.83	14.76	15.28	15.21
$Fe_2O_3^T$	1.42	1.62	1.87	2.72	1.67	1.48	2.57	3.26
MnO	0.18	0.19	0.20	0.09	0.07	0.09	0.08	0.13
MgO	0.22	0.26	0.25	0.76	0.46	0.41	0.67	0.81
CaO	0.63	0.71	0.67	2.68	1.75	1.63	2.61	2.75
Na_2O	4.21	4.74	4.16	3.97	3.57	4.65	3.95	4.11
K_2O	4.68	4.55	4.91	3.12	4.79	2.87	3.31	3.44
P_2O_5	0.05	0.06	0.05	0.09	0.06	0.06	0.08	0.09
L.O.I	0.34	0.47	0.31	0.28	0.40	0.55	0.43	0.25
Total	99.87	99.87	99.87	99.87	99.87	99.87	99.87	99.87
A/CNK	1.07	1.03	1.07	1.02	1.04	1.08	1.03	0.98
Sc	3.46	3.16	2.73	4.41	6.14	5.72	4.72	4.22
V	5.31	6.74	5.94	33.7	22.2	21.0	34.3	28.7
Cr	6.86	11.9	25.5	100	112	115	125	14.2
Ni	2.97	1.98	2.55	5.75	6.37	6.29	6.19	2.40
Rb	145	149	135	85.3	119	111	79.4	91.4
Sr	49.7	53.7	47.5	294	211	200	309	327
Y	17.8	26.6	19.7	17.1	12.3	16.2	12.8	20.1
Zr	29.9	49.7	33.1	75.5	53.4	59.7	67.3	56.9
Nb	11.8	11.2	7.84	6.13	5.26	13.0	5.32	9.12

Cs	5.60	4.46	4.95	3.85	2.65	4.03	7.60	3.70
Ba	75.6	70.6	75.3	484	390	430	547	415
La	6.91	8.11	8.06	20.9	15.8	13.8	13.0	11.6
Ce	15.7	19.2	18.6	42.0	30.6	27.2	25.3	23.6
Pr	1.91	2.42	2.30	5.07	3.65	3.27	3.08	2.95
Nd	6.86	8.63	8.22	19.3	12.8	11.6	11.5	11.6
Sm	1.95	2.53	2.36	3.90	2.48	2.57	2.27	2.80
Eu	0.10	0.11	0.10	0.67	0.51	0.44	0.66	0.65
Gd	1.96	2.87	2.43	3.42	2.37	2.58	2.21	2.68
Tb	0.41	0.63	0.50	0.51	0.37	0.45	0.34	0.49
Dy	2.78	4.22	3.20	2.91	2.10	2.81	1.99	3.12
Ho	0.56	0.82	0.62	0.60	0.43	0.50	0.42	0.69
Er	1.40	1.93	1.46	1.74	1.05	1.20	1.28	1.92
Tm	0.21	0.27	0.21	0.27	0.16	0.18	0.20	0.32
Yb	1.26	1.56	1.23	1.90	1.10	1.21	1.53	2.23
Lu	0.16	0.20	0.16	0.32	0.18	0.20	0.28	0.36
Hf	1.62	2.59	1.78	2.45	1.82	2.17	2.12	2.20
Ta	0.97	0.98	1.43	0.67	0.69	1.35	0.55	1.12
Pb	20.6	19.5	30.3	21.4	28.2	22.6	20.9	21.7
Th	3.81	5.38	5.40	5.73	5.33	6.41	5.02	4.59
U	0.92	2.59	3.74	4.95	1.47	2.79	1.44	1.99
Eu/Eu*	0.16	0.12	0.13	0.56	0.64	0.52	0.90	0.72
T_{Zr}(℃)	598	630	604	660	636	652	651	629

O_3^T = Total Fe_2O_3 content; $Mg^{\#}$= molecular $Mg^{2+}/(Mg^{2+}+Fe^{2+})\times100$; A/CNK = $(Al^{3+}/[Ca^{2+} + K^{2+} + Na^{2+}])$; Eu/Eu* = $Eu_N/(Sm_{CN}\times Gd_{CN})^{1/2}$; subscript CN presents chondrite normalization, the chondrite normalization values are from Sun & McDonough (1989). T_{Zr} are calculated after Boehnke et al. (2013).

bbreviations as in Table 1.

Table 3 Sr and Nd isotope data for the Zhengga leucogranites and associated rocks

		Rb	Sr	Sm	Nd	$^{87}Rb/^{86}Sr$	$^{87}Sr/^{86}Sr\pm2\sigma$	$(^{87}Sr/^{86}Sr)_i$	$^{147}Sm/^{144}Nd$	$^{143}Nd/^{144}Nd\pm2\sigma$	T_{2DM} (Ga)	$(^{143}Nd/^{144}Nd)_i$	$\varepsilon_{Nd}(t)$
09TB66	GBG	127	51.5	2.43	8.30	7.16	0.711362±2	0.704957	0.177	0.512652±8	1.08	0.512579	+0.43
11SR01-1	GBG	127	29.6	1.94	7.02	12.4	0.714894±5	0.703770	0.167	0.512663±3	1.04	0.512594	+0.73
11SR01-2	GBG	147	36.4	2.51	8.56	11.7	0.714156±5	0.703683	0.177	0.512660±3	1.06	0.512587	+0.59
11SR01-3	GBG												
11SR05-2	GBG	142	49.5	2.43	8.06	8.33	0.711200±5	0.703845	0.183	0.512660±3	1.07	0.512585	+0.54
11SR05-3	GBG												
16ML06-1	GBG								0.171	0.512667±5	1.04	0.512598	+0.77
16ML06-2	GBG												
16ML07-1	GBG								0.169	0.512666±4	1.04	0.512598	+0.77
16ML08-1	GBG												
16ML08-2	GBG	149	53.7	2.53	8.63	8.03	0.711362±8	0.704289	0.177	0.512666±4	1.05	0.512594	+0.70
16ML09-1	GBG	135	47.5	2.36	8.22	8.21	0.711433±13	0.704201	0.174	0.512653±7	1.08	0.512582	+0.47
11SR03	BG												
11SR04	BG	119	211	2.48	12.8	1.63	0.706379±5	0.704918	0.118	0.512631±4	1.07	0.512582	+0.49
11SR05-1	BG												
11SR06	BG	79	309	2.27	11.5	0.742	0.705642±4	0.704978	0.119	0.512633±4	1.07	0.512584	+0.53
16ML02-1	BG	91	327	2.80	11.6	0.808	0.705625±12	0.704914	0.146	0.512676±4	0.99	0.512617	+1.15
11SR02-1	TMG	209	142	4.90	22.8	4.24	0.727320±8	0.723584	0.130	0.512039±3	1.78	0.511986	-11.1
11SR02-3	TMG	254	131	5.40	26.4	5.60	0.732303±8	0.727373	0.124	0.512044±3	1.77	0.511993	-11.0

$Rb/^{86}Sr$ and $^{147}Sm/^{144}Nd$ are calculated using whole-rock Rb, Sr, Sm and Nd contents in Table 1.

$(t) = [(^{143}Nd/^{144}Nd)s/(^{143}Nd/^{144}Nd)_{CHUR}-1]\times10000$. $T_{2DM}=\ln\{[\varepsilon_{Nd}(t)-\varepsilon^{DM}_{Nd}(t)]/[(f_C-f_{DM})]+e^{\lambda t}\}/\lambda$ (Liew & Hofmann, 1988).

n the calculation, $(^{143}Nd/^{144}Nd)_{CHUR}=0.512638$, $(^{147}Sm/^{144}Nd)_{CHUR}=0.1967$, $(^{143}Nd/^{144}Nd)_{DM}=0.513151$, $(^{147}Sm/^{144}Nd)_{DM}=0.2135$, $(^{147}Sm/^{144}Nd)_{CC}=0.12$, $\lambda_{Sm}=6.54\times10^{-12}$/yr and t=63 Ma.

Abbreviations as in Table 1.